2022

A Combined Spectral and Energy Morphology Analysis of Gamma Ray Source HAWC J2031+415 in the Cygnus Constellation

Ian Herzog
Michigan Technological University, igherzog@mtu.edu

A COMBINED SPECTRAL AND ENERGY MORPHOLOGY ANALYSIS OF GAMMA RAY SOURCE HAWC J2031+415 IN THE CYGNUS CONSTELLATION

By

Ian G. Herzog

A THESIS

Submitted in partial fulfillment of the requirements for the degree of

MASTER OF SCIENCE

In Physics

MICHIGAN TECHNOLOGICAL UNIVERSITY

2022

This thesis has been approved in partial fulfillment of the requirements for the Degree of MASTER OF SCIENCE in Physics.

Department of Physics

Thesis Advisor: *Dr. Petra Huentemeyer*

Committee Member: *Dr. Brian Fick*

Committee Member: *Dr. Elena Giusarma*

Department Chair: *Dr. Ravindra Pandey*

Contents

List of Figures

List of Tables

List of Abbreviations

AS	Air Shower
ASPD	Air Shower Particle Detectors
ARGO	Astrophysical Radiation with Ground-based Observatory
BIC	Bayesian Information Criterion
CR	Cosmic Ray
DBE	Diffuse Background Emission
eV	Electron Volt
GeV	Gigaelectron volt
GP	Ground Parameter
HAWC	High-Altitude Water Cherenkov
HEGRA	High-Energy-Gamma-Ray Astronomy
IACT	Imaging Atmospheric Cherenkov Telescopes
IC	Inverse Compton
ISM	Interstellar Medium
KN	Klein-Nishina
Kyr	Kiloyear
LHAASO	Large High Altitude Air Shower Observatory
MAGIC	Major Atmospheric Gamma Imaging Cherenkov Telescopes

MeV	Megaelectron Volt
NN	Neural Network
PeV	Petaelectron volt
PMT	Photomultiplier Tube
PS	Point Source
PSR	Pulsar
PWN	Pulsar Wind Nebula
ROI	Region of Interest
RPC	Resistive Plate Chambers
SNR	Supernova Remnant
TeV	Teraelectron Volt
VERITAS	Very Energetic Radiation Imaging Telescope Array System
VHE	Very High Energy
WC	Water Cherenkov

Abstract

HAWC J2031+415 is a probable pulsar wind nebula (PWN) located in the Cygnus Cocoon region near a complex OB star cluster. First observed by the High-Energy-Gamma-Ray Astronomy (HEGRA) observatory in the TeV energy regime, the source had no apparent counterpart in lower energy ranges. Previous work using 1343 days of data from the High-Altitude Water Cherenkov (HAWC) Gamma-Ray Observatory has determined that three sources are present in the Region of Interest (ROI): HAWC J2031+415, HAWC J2030+409 (also known as the Cocoon), and 3HWC J2020+403 (associated with the Gamma Cygni supernova remnant) [14, 15].

In this work, I use the newest data set containing 2000 days of data from HAWC to analyze the region. I apply a systematic source searching method to determine the number of sources, their locations, and spectra. Three estimators are used to determine the spectral energy distribution for HAWC J2031+415 and the best fit is found to be a power law with an exponential cut-off. I then isolate HAWC J2031+415 and perform an energy-dependent morphology study of the source. No measurable energy dependence of the morphology was found. Additional data will allow for more detailed studies of the region.

Chapter 1

An Introduction to High Energy Astrophysics

The field of astrophysics is defined as the study of extraterrestrial bodies and phenomena by observing and modelling their emission regions to discover the engines powering these regions[17]. The primary interface used to analyze these sources is the particles they emit, these being primarily hydrogen and helium, with heavier nuclei being more rare. These particles have a special name: cosmic rays (CR's), and they will be discussed further in Section 1.1. Section 1.2 will delve into the acceleration of CR's, Section 1.3 will discuss gamma ray production, and Section 1.4 will discuss the emission regions where these particles and gamma rays are emitted from.

1.1 High-Energy Astrophysics and Cosmic Rays

In order to discuss any in-depth analysis of HAWC J2031+415, an understanding of both CR's and their main acceleration mechanism at high energies is required. The exact origin of individual CR's is unknown except it is believed that they come from some of the most extreme and energetic phenomena in the universe. As CR's are the nuclei of atoms, they are deflected by nearby magnetic fields and hit Earth from all directions. It is estimated that approximately 1000 CR's per meter per second hit Earth's atmosphere and while most have energies comparable to their rest mass, approximately 10^8 electron volt (eV), some have energies up to 10^{20} and beyond [18]. It is from these very high energy (VHE) CR's that produce 0.1-100 tera-electronvolt (TeV) gamma rays. As seen in Figure 1.1, gamma rays have energies of 10^6 eV and gamma rays with $E > 10^{11}$ eV are what the High-Altitude Water Cherenkov Gamma-Ray Observatory (henceforth referred to as "HAWC") detects.

1.2 Cosmic Ray Acceleration

There are certain mechanisms that allow CR's to be accelerated to the VHE regime. The primary method that will be addressed here is First Order Fermi Acceleration. It is currently believed that this acceleration process is responsible for most cosmic

Electromagnetic Spectrum

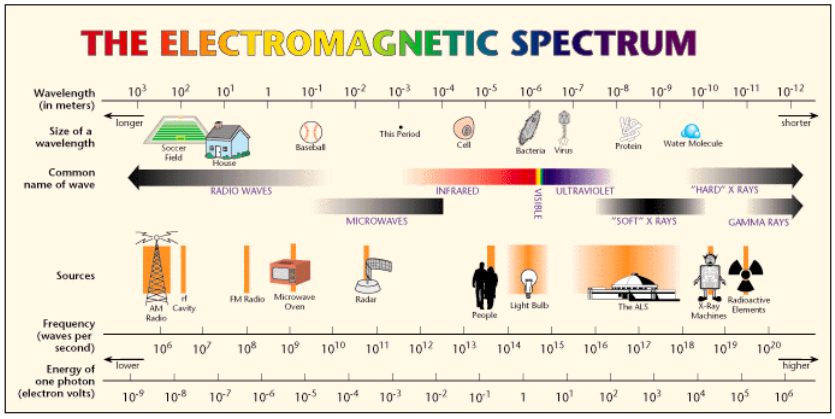

Figure 1.1: The energy spectrum. Used with permission from [1].

ray acceleration [19]

1.2.1 Fermi Acceleration

First Order Fermi Acceleration (referred to henceforth as "Fermi acceleration") is an efficient acceleration method for cosmic rays refers to particle acceleration in shock fronts. This acceleration method functions by having a particle travelling at relativistic speeds enter a shock wave. The origins of these shock waves will be discussed in more detail in Section 1.4.

The process for Fermi acceleration is visualized in Figure 1.2. The shock front travels with velocity U and the surrounding gas "flows" into the shock front with the same velocity and then flows out of the front with velocity U/4. From the frame of the

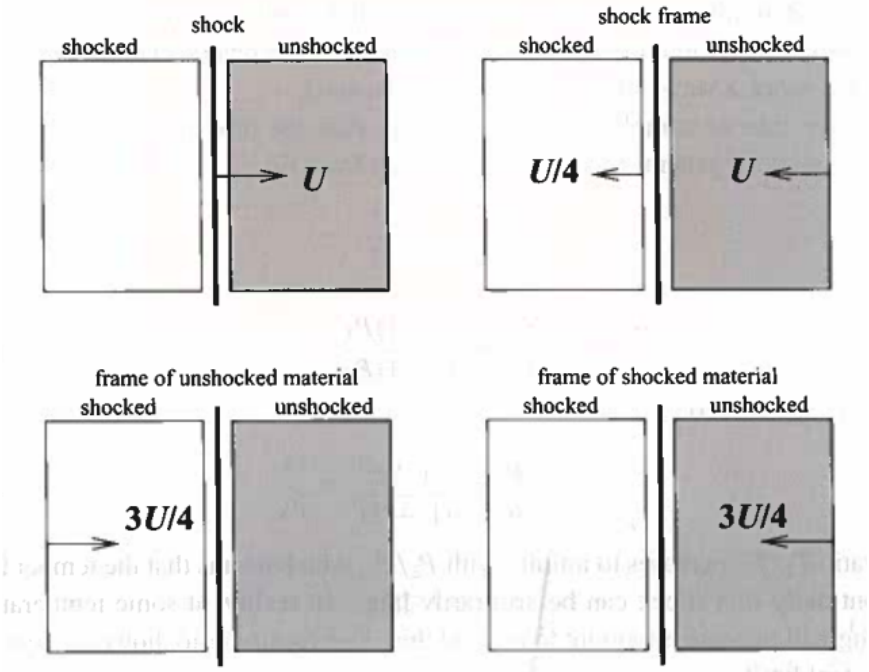

Figure 1.2: First order Fermi Acceleration. Used with permission from [2].

unshocked gas, the shocked material moves with velocity 3U/4. Consider a fast particle in the unshocked frame entering the shocked frame with momentum $p = E/c$. It interacts with magnetic eddies generated by plasma interactions with shocked and unshocked material. The particle gains energy by reaching equilibrium with the surrounding material. Assuming a Lorentz factor of 1 (nonrelativistic shock), the fast particle's change of energy is given in terms of the constant β:

$$E = \beta E_o \tag{1.1}$$

Whenever a particle crosses the shock front it experiences this same fractional increase

and, given the complex nature of the magnetic fields and macro structure of the shock fronts, this particle has the potential to repeatedly cross this front and obtain very high energies. The question now is what kind of energy spectrum is produced from this acceleration?

Considering Equation 1.1, after the particle has j crossings it's energy is

$$E = E_o \beta^j \tag{1.2}$$

Now, a particle also has the probability P of staying in the shock region. The total number of particles left in the region after j crossings is

$$N = N_o P^j \tag{1.3}$$

Taking the ratio of N and E and taking the log to remove the j exponential yields

$$\frac{\log N/N_o}{\log E/E_o} = \frac{\log P}{\log \beta} \tag{1.4}$$

Solving Equation 1.4 for N/N_o givens our final expression for our energy spectrum:

$$\frac{N}{N_o} = (\frac{E}{E_o})^{\frac{\log P}{\log \beta}} \tag{1.5}$$

It is convenient to write Equation 1.5 in differential form and for now consider the proportional relationship between N and E

$$N(E)\mathrm{d}E \propto E^{\log P/\log \beta - 1} \propto E^{-k}\mathrm{d}N \tag{1.6}$$

where k is defined as the power law index of this energy spectrum. As this is a non-thermal distribution, there is no exponential drop-off. The specifics of k's derivation can be found in [2, 19, 20] while a brief explanation of the process is provided. While the shock is assumed to be non-relativistic, the particles contained within the shock fronts are not. From one complete trip (upstream to downstream and back), a given particle has an average energy increase of $2 * (2V)/(3c)$ [20]. Therefore, β is given by

$$\beta = \frac{E}{E_o} = 1 + \frac{4V}{3c} = 1 + \frac{U}{c} \tag{1.7}$$

And probability that the particle returns to the upstream region is given by $P = 1 - U/c$. Solving for $\log P$ and $\log \beta$ gives

$$\log P = \log(1 - \frac{U}{c}) = -\frac{U}{c} \quad \text{and} \quad \log \beta = \log(1 + \frac{4V}{3c}) = \frac{U}{c} \tag{1.8}$$

Substituting into Equation 1.6 gives the final result

$$N(E)\mathrm{d}E \propto E^{-2}\mathrm{d}E \tag{1.9}$$

When compared to experimental observations, k trends towards a softer (faster decay of high energy events) 2.7 [21]. This can partially be corrected by relaxing assumptions made in the derivation [2]. This acceleration method is responsible for the vast majority of accelerated cosmic rays.

1.3 Gamma Ray Production Mechanisms

There are 2 production mechanism classes considered here: hadronic (protons) and leptonic (electrons). One mechanism from each dominants in the production of TeV gamma-rays and their basic mechanisms will be introduced in the following sections. Additionally, a lower energy (MeV, GeV) production method for leptonic particles is introduced and will be used in further discussion in Chapter 3

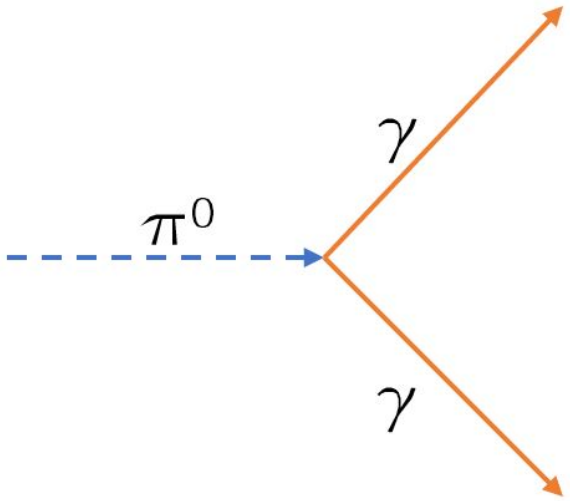

Figure 1.3: Pion decay resulting in 2 gamma rays

1.3.1 Neutral Pion Decay

The main hadronic gamma ray production method is called neutral pion decay (π^0 decay) and its process can be seen in Figure 1.3. The pions are produced from protons or nuclei inelastically colliding with surrounding medium and have a mean lifetime of the order of 10^{-16} seconds, after which they decay into two gamma rays. Given the threshold energy needed to produce neutral pions (280 MeV) and the large amount being produced, this production mechanism can form a "pion bump" in the GeV-TeV spectrum range [9, 22].

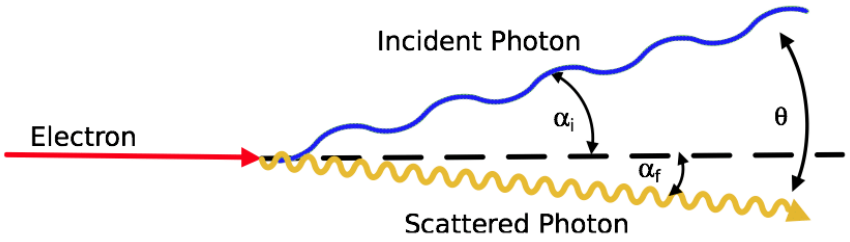

Figure 1.4: Inverse Compton scattering. The angles are relevant for the derivation and are beyond the scope of this thesis. Used with permission from [3].

1.3.2 Inverse Compton Scattering

Inverse Compton (IC) scattering is the process in which an ultra relativistic electron collides with a low energy photon and increases the photon's energy to the gamma ray regime. The specific process is shown in Figure 1.4. It is effective for a wide variety of emission regions and is highly efficient in low magnetic fields and gas densities in the interstellar medium (ISM) [9]. The scattering cross-section of the IC process can be expressed as a function of the electron energy E_e and the photon's initial energy $w_o = h\nu$ with the term $\epsilon_o = w_o/E_e$. This equation is called the Klein-Nishina (KN) equation [9, 22],

$$\sigma_{IC} = \frac{3\sigma_T}{8\epsilon_o}[(1 - \frac{2}{\epsilon_o} - \frac{2}{\epsilon_o^2})\ln(1 + 2\epsilon_o) + \frac{1}{2} + \frac{4}{\epsilon_o} - \frac{1}{2(1 + 2\epsilon_o)^2}] \tag{1.10}$$

Where σ_T is the Thomson scattering cross-section and is given by $\sigma_T = (8\pi/3)r_e^2$ and

r_e is the radius of an electron. This expression can yield two different differential cross sections depending on the frequency of light emitted. At lower frequencies (visible light), $\epsilon_0 \ll 1$ and non-relativistic electrons produce Thomson scattering while at higher frequencies, $\epsilon_o \gg 1$ and relativistic electrons produce Compton scattering. The latter is also known and the KN regime [23].

In addition to the cross section, the energy loss rate for both Thomson and KN regimes can be found and these are shown in Equations 1.11 and 1.12 respectively [9].

$$\frac{-dE_e}{dt} = \frac{4}{3}\sigma_T c \omega_o n_{ph} E_e^2, \quad b \ll 1 \tag{1.11}$$

$$\frac{-dE_e}{dt} = \frac{3}{8}\frac{\sigma_T c n_{ph}}{\omega_o}(\ln b - 11/6), \quad b \gg 1 \tag{1.12}$$

Where n_{ph} is the number density of photons and $b = 4\epsilon_o$. From Equations 1.11 and 1.12 it can be seen that while in the Thomson regime the energy loss is proportional to E_e^2, for the KN regime it is almost energy independent. These expressions imply that for the Thomson regime the steady-state electron spectrum becomes steeper while for the KN regime emitted photons suffer a very sharp cutoff. One final note is that while protons go through the IC process as well, the rate of proton interaction is proportional to $(m_e/m_p)^4$ and so is not significant enough to consider [22].

1.3.3 Synchrotron Emission

There is a second leptonic emission method that will be briefly introduced here: synchrotron emission. When an electron moves through a magnetic field, it gets accelerated and follows a spiral trajectory. When this happens, the electrons emit low energy gamma rays (MeV, GeV) through synchrotron radiation, so-called named because of the path taken. If the electrons travel along curves in the magnetic field rather than spirals, curvature radiation is produced instead. This emission is too low energy for HAWC to see but it is important to pulsar wind nebulae, as discussed in Chapter 4.

1.4 Emission Regions

This last section will consider galactic gamma ray emission regions only. While there are many known extra-galactic sources, few are visible to HAWC and my analysis on HAWC J2031+415 is strictly galactic in nature. There are 3 relevant gamma ray source classes for this analysis and they are introduced here.

1.4.1 Supernova Remnants (SNRs)

A SNR is what remains after a star $M > 8M_o$ experiences total core collapse when it runs out of fusion material (hydrogen, then helium and heavier elements). These are among the most energetic phenomena currently know and can outshine entire galaxies. When a star goes supernova, it ejects vast amounts of material that sweeps up the surrounding ISM. This creates the SNR and this region will continue expanding until it fully merges with the ISM. A more complete discussion on the steps this process follows can be found here [24]. As the SNR expands, the ejected material compacts the ISM, generating shock fronts and allowing Fermi acceleration to occur.

1.4.2 Pulsar Wind Nebulae (PWN)

When a SNR is created, it has the possibility to become a Pulsar Wind Nebula (PWN). A PWN is an SNR that is powered by a pulsar, a special case of a neutron star that has a rapid rotation period and strong magnetic fields. PWN can be modelled as non-aligned magnets with very large magnet moments that is surrounded by a magnetosphere [9]. The pulsar generates a wind that contains electrons and positrons emitted from the pulsar and contribute to its slowing rotation. The power emitted from a pulsar is given by [2]

$$\frac{dE_{rot}}{dt} = I\omega\dot{\omega} \tag{1.13}$$

Where I is the moment of inertia of the pulsar, ω is the angular frequency, and $\dot{\omega}$ is the deceleration rate. The pulsar's characteristic or dipole age can be determined by

$$\tau_{dipole} = \frac{P}{\dot{P}} \tag{1.14}$$

Where P is the rotational period of the pulsar and $\dot{P}$ is the change in that rotation. When the high energy electrons reach the shock front termination and enter into the ISM they inverse Compton scatter with the ambient photons and produce gamma rays [9]. PWNs will be discussed in more detail in Chapter 3

1.4.3 Star Birthing Regions

Star birthing regions have also been theorized to produce gamma ray emission [25]. These structures produce gamma rays using several different methods. The relevant for the Cygnus region relies on the acceleration of particles to relativistic energies through stellar winds being combined from the stars and SNRs within the region [25, 26]. These particles then interact with the ISM or the surrounding star birthing

region, causing a wide region to emit gamma rays. One key aspect of this emission region is that it can suppress emission at low energies, resulting in TeV sources with no lower energy counterpart [25].

These three source types are present in my analysis of HAWC J2031+415 and the specific sources will be discussed more in Chapter 5.

Chapter 2

Gamma Ray Observatories

Observed gamma rays are spread across 9 decades, from MeV (10^6eV) to recently observed PeV (10^{15}eV) events from the Large High Altitude Air Shower Observatory (LHAASO) [27, 28]. To observe this wide energy spectrum, both space and ground-based observatories are used. This chapter will focus on ground-based observatories and introduce the HAWC array along with its basic analysis framework.

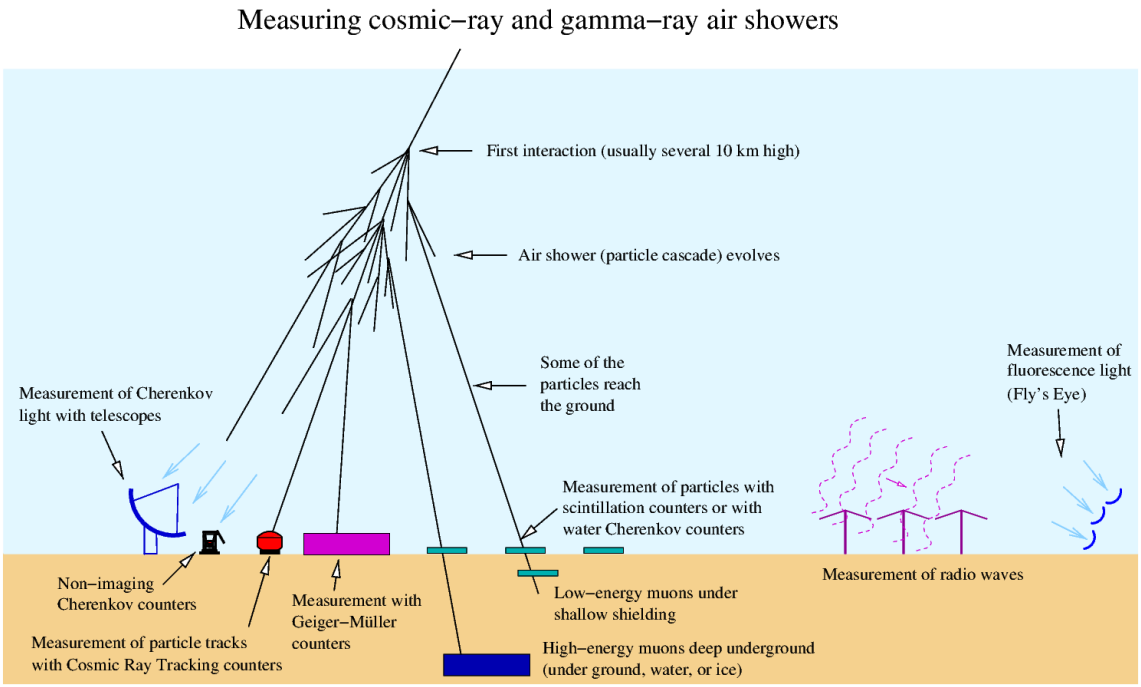

Figure 2.1: An example of an EAS. Used with permission from [4].

2.1 Extensive Air Showers

When primary particles (gamma rays, hadrons, etc.) enter Earth's atmosphere, they interact with atmospheric molecules, creating an electron-positron pair. These secondary particles produce gamma rays via bremsstrahlung and these new gamma rays continue the interaction chain [28]. This process, called an Extensive Air Shower (EAS), can be seen in Figure 2.1.

As it can been seen, after first contact with the atmosphere, a cascade of particles (mostly nuclear fragments) and photons (gamma rays) shower down onto Earth's surface. Depending on the primary particle, two different shower types are produced:

electromagnetic and hadronic showers. Electromagnetic EAS's are formed when a high energy electron, positron (positively charged electron), or photon enters the atmosphere. When this happens, an electron-positron pair is produced and cascades through the upper atmosphere, interacting with matter and producing more electron-positron pairs until a critical energy threshold is reached. When the electron-positron energy reaches 80 MeV, the cascade stops expanding and the secondary particles produced rapidly drops due to ionization losses [15, 28]. This point is called the shower maximum. Once the shower hits gamma ray observatories like HAWC they reconstruct the shower and allows the analysis of the parent sources.

By contrast the hadronic shower is caused when a hadron (typically protons or neutrons) encounters the upper atmosphere. Approximately half the hadron's energy is transferred to secondary particles produced by collisions while the other half is consumed by particle production of slow pions. Some of the produced pions are π^0 which decay into two gamma rays (as discussed in Chapter 1) and produce electromagnetic EAS's. Hadronic showers develop slower than electromagnetic showers and the distinction between gamma and hadron showers is key for HAWC's data collection process.

There are 2 kinds of observatories that observe these showers: Imaging Atmospheric Cherenkov Telescopes (IACTs) and Air Shower Particle Detectors (ASPDs). Some IACTs and ASPDs use a special property of light: Cherenkov radiation and, given

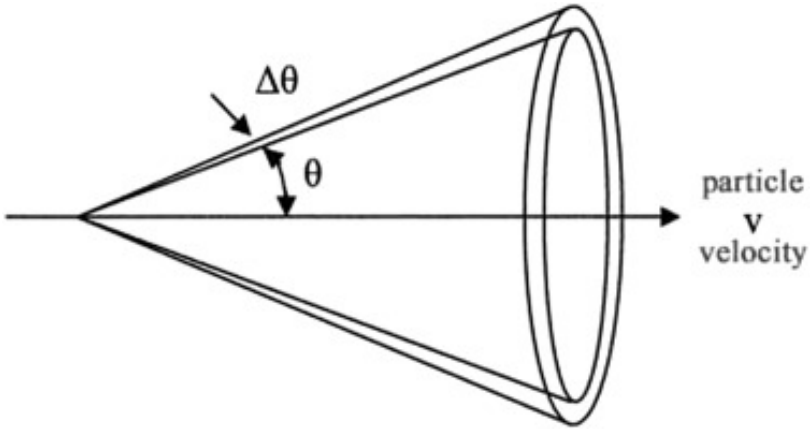

Figure 2.2: Propagation of Cherenkov radiation through a medium. Used with permission from [3].

its importance, it will discussed in Section 2.1.1.

2.1.1 Cherenkov Radiation

Cherenkov radiation is emitted when a charged particle (neutral particles do not experience this phenomenon) passes through a medium at a velocity greater than the phase velocity of light in that medium. When Cherenkov radiation is emitted, it forms a cone of radiation emitted from the particle as it passes through the medium, as seen in Figure 2.2. Cherenkov radiation is primarily used by ASPDs to record EAS's while IACTs focus on Cherenkov light emitted by showers to collect data. Additionally, ASPDs use other detection methods besides Cherenkov radiation to detect and are discussed in Section 2.3.

Cherenkov radiation detection is dependent on the half angle made by the cone of

light produced by the travelling particle. The angle θ is given by:

$$\cos\theta = \frac{1}{\beta \mathrm{n}} \tag{2.1}$$

Where β is the particle's velocity as a fraction of the speed of light and n is the refractive index of the interface. For water, n = 1.33 and the emission angle is $\leq 42^\circ$ [29]. This angle is crucial in designing water tanks to ensure that the light is accurately detected.

2.2 Imaging Atmospheric Cherenkov Telescopes

IACTs function by detecting Cherenkov radiation with a large mirror array (similar to a refracting telescope). They use high speed cameras to photograph the EAS as it travels through the atmosphere. They have the ability to aim across a wide range of the sky, though it is important to acknowledge that they do not see the entire viewable sky simultaneously. An example of an IACT is the Very Energetic Radiation Imaging Telescope Array System (VERITAS), see Figure 2.3. VERITAS is composed of four 12 meter IACT telescopes that combined have an effective area of .1 km^2 at 1 TeV [30]. It also has very good angular resolution at $\leq 0.05^\circ$ for photons.

Figure 2.3: The VERITAS observatory. Used with permission from the Smithsonian Astrophysical Observatory [5].

The advantage of IACTs is their smaller angular resolution but they suffer by having a small field of view. In VERITAS' case its field of view is 3.5°. Additionally, they also can only collect data under clear skies and mostly moonless nights.

Another example for an IACT relevant for the work presented in this thesis is the Major Atmospheric Gamma Imaging Cherenkov Telescopes (MAGIC) system located on La Palma, one of the Canary Islands. MAGIC consists of two 17 meter diameter IACTs with an energy range of 50 GeV to $>$ 30 TeV. The first telescope was constructed in 2003 with the second operational in 2009 [31, 32].

Finally, the first IACT conducting a deep gamma ray survey of the Cygnus constellation is the High-Energy-Gamma-Ray Astronomy (HEGRA) telescope array. HEGRA was located on the same island as MAGIC and was MAGIC's predecessor, operating from 1997 to 2002. This array was composed of 5 Cherenkov telescopes with 8.5 m^2 surface area. This gave HEGRA an effective energy range of 0.5 to $>$ 50 TeV.

HEGRA is notable for being the first to discover TeV J2032+4130, a TeV source that had no clear association in lower energy regimes at the time [10].

2.3 Air Shower Particle Detectors

By contrast, ASPDs require air showers to reach the ground where the detectors are installed to be detected and so are built at higher elevations. The shower maximum depends on the initiating particle and occurs on average at or above 5000 meters [15]. ASPDs have an angular resolution that is worse than IACTs ($\approx 0.1^{\circ}$) and cannot distinguish point sources as well as IACTs. However, the advantage of ASPDs is that they have much higher up time because they do not rely as much on atmospheric conditions to collect data. Additionally, they have much larger fields of view than IACTs.

There are several ways that ASPDs collect data. The first method, scintillation counters, is used by the Tibet Air Shower Gamma Experiment (Tibet AS). Located in Yangbajing, China, this array has been operational using scintillation counters since 1990 [33]. Scintillation is a process in which light is emitted when a particle interacts with a medium and the counter component detects this flash. Usually the detector component is a photomultiplier tube (PMT) to boost the signal [34].

A second method is Resistive Plate Chambers (RPCs) and is used by the Astrophysical Radiation with Ground-based Observatory (ARGO) in Yangbajing, China. RPCs consist of two parallel plates, a positive anode plate and negative cathode plate. These plates are separated by a gas and, when a muon passes through the gas, electrons get knocked out of orbit. This in turn creates a cascade of electrons that are transparent to the electrodes, allowing them to pass through and be measured by a series of detector strips that collect the relevant data about the muon and corresponding shower [35, 36].

The third detection mechanism is Water Cherenkov (WC) detectors. The general principle of WC arrays is that the detectors are submerged in water and detects Cherenkov radiation. The water and WC detectors can either be in self-contained tanks like with HAWC, the WC detectors can be placed in a large pond like with HAWC's predecessor MILAGRO [37], or a combination of the two with LHAASO. The functionality of HAWC will be discussed in further below. It should be noted that LHAASO is a hybrid array with both WC and IACT-style detectors.

2.4 HAWC Array

The HAWC array is located Sierra Negra, Mexico at an altitude of 4100 meters. The main array is composed of 345 tanks and can be seen in Figure 2.4. Each of these

Figure 2.4: An aerial shot of the HAWC array. The large tanks are the main array while the smaller tanks are part of the outrigger array. The off-center building at the array's core is the counting house. The outriggers are currently not considered for data collection. Photo courtesy of Dr. Jordan Goodman of the HAWC collaboration.

tanks has a 7.3 meter diameter with a depth of 4.5 meters. The individual tank volume is approximately 200,000 liters filled with purified water. Inside each tank are four PMTs, three of which are 8-inch Hamamatsu R5912 models that are placed in a triangular formation around the single high-quantum efficiency 10-inch Hamamatsu R7081-MOD [38]. This configuration can be seen in Figure 2.5

Additionally, Figure 2.5 also details the process of how events are detected with

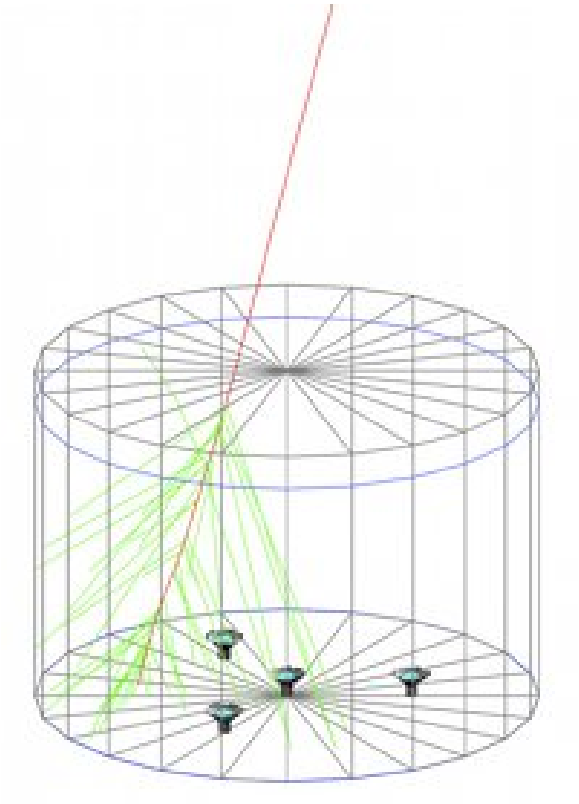

Figure 2.5: The layout of each WC detector. The red line indicates a charged muon and the green cascade is the Cherenkov light that particle emits when interacting with the water. Photo from `https://www.hawc-observatory.org/observatory/tanks.php`

HAWC. When a suitably high enough energy particle enters the WC tanks, the resulting cascade of Cherenkov light is detected by the PMT's present. When the PMT's detect this light, it converts it to photoelectrons in accordance with the photoelectric effect. This signal is then greatly amplified by a factor of $\approx 10^7$ and sent through to the counting house seen at the center of the main array in Figure 2.4 and analyzed.

Chapter 3

Pulsar Wind Nebulae and HAWC J2031+415

This chapter will discuss the formation process and characteristic modelling of pulsars and their surrounding nebulae, as well as considering the gamma ray emission related to these objects. Additionally, PSR J2032+4127, the pulsar believed to be associated with HAWC J2031+415, will be introduced.

3.1 Stellar Death

Stars prevent gravitational collapse by compressing their cores to the point that nuclear fusion becomes possible. Hydrogen gas is fused to produce helium and this process produces enough thermal energy to reach an equilibrium point with the gravitational force. As a star nears the end of its hydrogen supply, the fusion rate slows and its core contracts. Due to the increased pressure, conditions for helium fusion becomes favorable. What happens next is dependant on the star's mass, the amount of hydrogen in the outer layers, and the amount of helium in the star's core.

If a star has a mass $M < 10M_o$ (M_o is the mass of the sun), its most probable fate is to become a planetary nebula. This is where the star expands into a red giant and loses its shells in a series of shell flashes, throwing them out around the star core. The core collapses until electron degeneracy pressure halts the collapse and a white dwarf is created [39]. For stars with masses $10M_o < M < 26M_o$ electron degeneracy pressure is not sufficient to overcome the gravitational pressure and electrons are forced into protons, creating neutrons. Neutron degeneracy pressure is now the dominating force and counteracts gravitational pressure, creating a neutron star [6, 39]. Stars with mass $M > 25M_o$ have gravitational forces so strong that neutron degeneracy is not enough to stop further core collapse and a black hole is created. The different progressions are summarized in Figure 3.1.

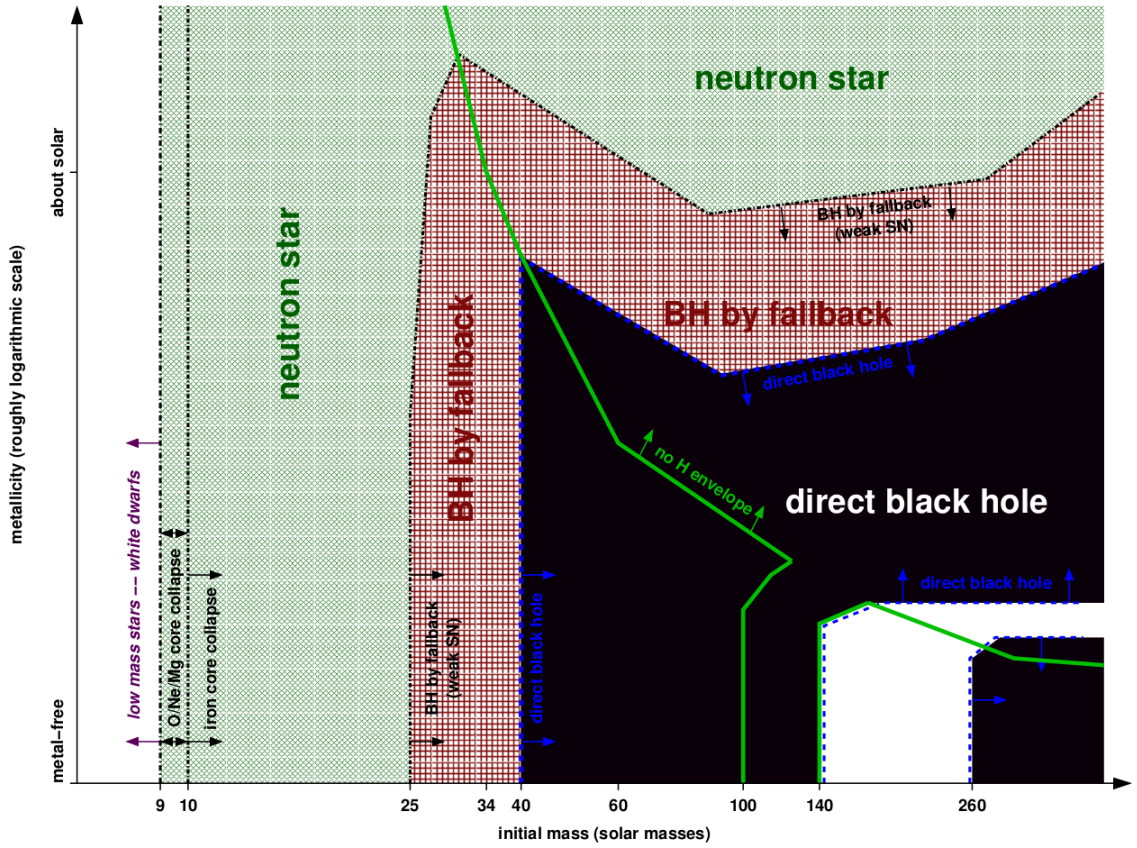

Figure 3.1: Diagram displaying the fate of stars from their mass [6].

3.2 Pulsar characteristics

Pulsars are a subclass of neutron stars that are characterized by their rapid, consistent rotation and the jets of radiation they give off at the magnetic poles. When a neutron star is formed, the angular momentum and magnetic flux of the parent star are preserved. While these characteristics are maintained, the radius of the parent star falls from hundreds of thousands of kilometers to tens of kilometers, causing a massive increase in the rotation period of the neutron star. The currently fastest rotating

pulsar known is PSR J1748−2446ad with a rotation rate of 716 Hz [40].

3.2.1 Spin-Down Luminosity and Pulsar Age

As shown in Equation 1.13, the spin-down luminosity of the pulsar is characterized by the energy-loss rate that the pulsar experiences. The energy loss $\dot{E}$ is on the order of 10^{28} to 10^{39} erg/s, though isolated PWN are only created with $\dot{E} > 10^{36}$ erg/s. If the pulsar is in a binary system then $\dot{E}$ can be as low at $\approx 10^{34}$ erg/s [41]. The parameters used to calculated the spin-down luminosity can also be used to determine the pulsar's age as shown in Equation 1.14 [2].

3.2.2 Surface Magnetic Field Strength

The magnetic field of a pulsar at its surface can be estimated using the rotation period and spin down rate P, $\dot{P}$ parameters and is given by:

$$B \approx 3.2 * 10^{19} (\frac{P\dot{P}}{1s})^{1/2}, \tag{3.1}$$

Where the momentum product has been normalized to 1 second. The range of magnetic field values for pulsars is approximately 10^8 to 10^{15} Gauss.

3.3 Gamma Ray Emission and Pulsars

As discussed in Section 3.2.2, pulsars have very strong magnetic fields that in turn generate strong electric fields. These electric fields are capable of pulling charged particles off the surface of the neutron star, specifically at the magnetic poles [9, 42]. It is believed that these charged particles are what cause electron-positron cascades which, in turn, form a particle plasma along the magnetic field lines and create the magnetosphere. The magnetosphere extends until the particles obtain a maximum speed (near the speed of light), forming a light cylinder that can be seen in Figure 3.1 [7, 9].

There are three models that model gamma ray emission from the magnetosphere and they all argue that the acceleration of electrons and positrons occur where the charged particle density, given by Equation 3.2, drops [43].

$$\rho_{GJ} = \frac{\Omega B}{2\pi c} \tag{3.2}$$

Here Ω is the angular momentum and B is the magnetic field. These emissions regions are the polar cap, slot gap, and outer gap regions [7, 9]. Both the polar cap and slot gap rely on strong acceleration near the poles to produce gamma rays via

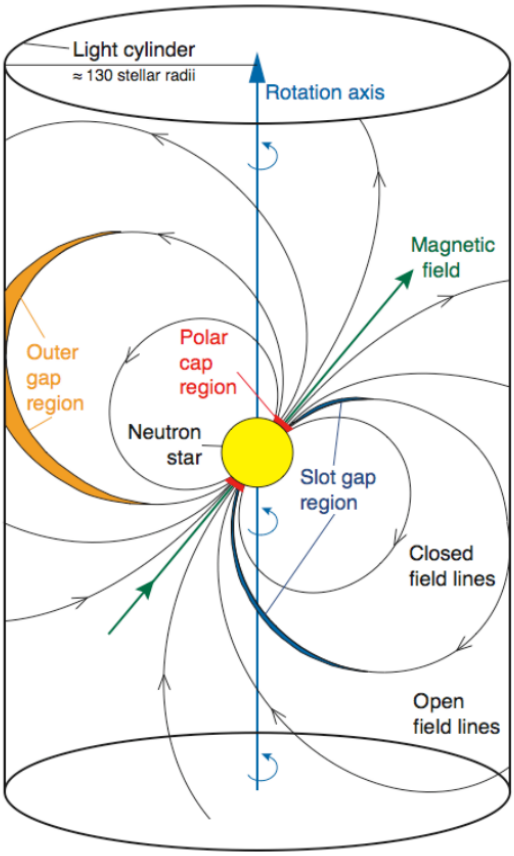

Figure 3.2: Outline of a pulsar and its magnetic field. Note the mis-aligned axes of rotation and magnetic field as this is what causes the "lighthouse" effect associated with pulsars. Additionally the polar cap, slot gap, and outer gap regions are highlighted. Photo taken from [7].

curvature radiation of electron-positron pairs [44, 45]. The polar cap model predicts this acceleration to be near the pole (≈30 km) while the slot gap model predicts acceleration on the closed magnetic field lines near the pulsar but away from the poles [9]. By contrast, the outer band gap acceleration occurs away from the pulsar where the magnetic field intensity has dropped by several orders of magnitude. Gamma rays here are produced either by IC scattering or curvature radiation [9, 22].

All gamma ray emission from the pulsar proper is produced in these three regions

and, as the pulsar rotates, is viewed as pulsed emission from Earth. This was first observed in the TeV energy range in 2008 with MAGIC [7] and, while internal studies with HAWC have been attempted, pulsation was not detected and therefore is not considered in this analysis.

3.4 Pulsar Wind Nebulae

PWNe are another by-product of SNRs. In this section both their formation and multi-wavelength emission will be explored.

3.4.1 Formation and Development

A PWN is part of a composite system, as shown in Figure 3.3, where the PWN is enveloped by the surrounding SNR. Though part of an SNR, a PWN does not significantly affect the total energy output of an SNR (primarily kinetic energy from the shock expansion phase) as a PWN's energy output is generally on the order of 100 times smaller than the SNR [46]. Given that energy disparity, an SNR is not significantly affected by the PWN's evolution but rather the PWN is highly dependent on the SNR's development.

After the initial supernova explosion, the SN enters a phase of free expansion that

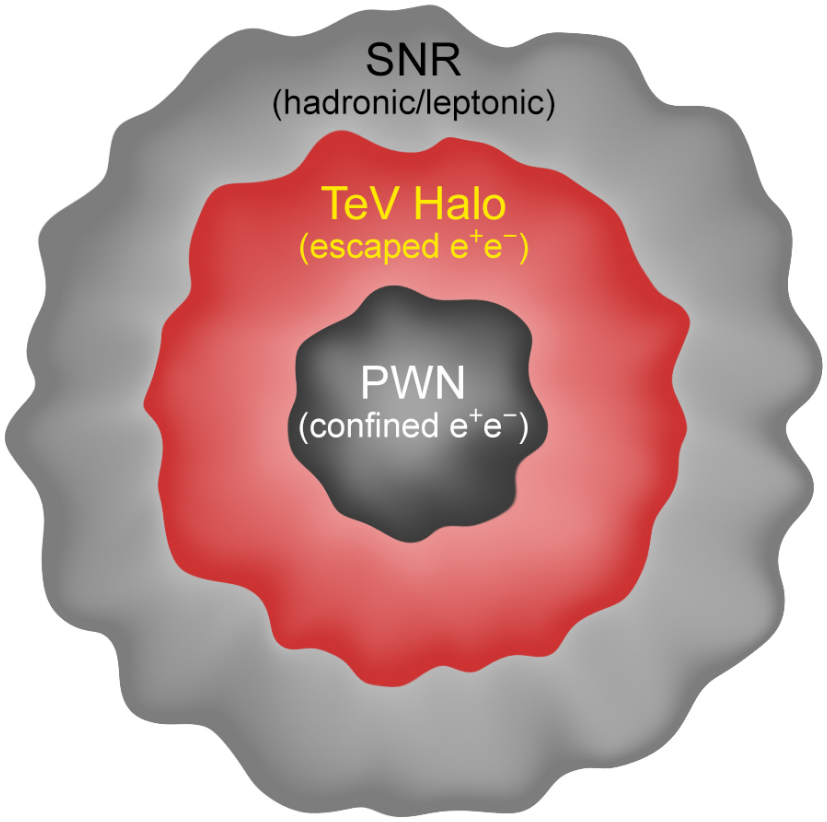

Figure 3.3: The general size comparison for an SNR vs a PWN. The SNR envelopes the PWN and constrains its growth through the SNR's development phases. TeV halos are an additional component of emission from SNR's and will not be discussed in this thesis. DOI:10.1103/PhysRevD.100.043016. [8]

lasts from 500-3000 years. The SNR expands with a velocity of $\approx 5 * 10^3$ km/s while the pulsar receives a significantly smaller kick velocity of $\approx$ 400 km/s. This kick velocity is caused by asymmetries in the supernova explosion. Therefore, for young SNRs, the pulsar remains near the center of the SNR. The PWN expands rapidly and, in the case of spherically symmetric expansion, the radius can be given by [46]:

$$R_{PWN} \approx 1.5 \dot{E}_o^{1/5} E_{SN}^{3/10} M_{ej}^{-1/2} t^{6/5}, \tag{3.3}$$

where $\dot{E}$ is the initial spin-down luminosity of the pulsar and E_{SN} and M_{ej} are the energy and mass ejected by the supernova.

After the free expansion phase, material that was initially accelerated by the supernova sweeps up the surrounds ISM and begins to decelerate. This deceleration causes shocks to form both on the expansion edge as well as inside the expanding material. These reverse shocks are caused by the more rapidly expanding material inside the SNR to collide with the slowing outer shells. This is the Sedov phase (also known as the Sedov-Taylor phase) and lasts for $\approx 10^4$ years. It is characterized by total energy being conserved and equally split by kinetic and thermal contributions [2, 46]. These reverse shocks eventually travel to the SNR center given by time t_{Sedov} [47]:

$$t_{Sedov} \approx 7 \left(\frac{M_{ej}}{10 M_o} \right)^{5/6} \left(\frac{E_{SN}}{10^{51} \text{ergs}} \right)^{-1/2} \left(\frac{n_o}{1 \text{cm}^{-3}} \right)^{-1/3} \text{kyr}, \tag{3.4}$$

where n_o is the number density of the ambient gas. If there is a pulsar at the center of the SNR, the collapsing reverse shock collides with the PWN's forward moving shock and compresses the PWN. This greatly increases pressure within the PWN and the compression rebounds with sudden expansion. The system oscillates for a

few thousands years and also results in significantly stronger magnetic fields being produced. After the oscillation subsides, the PWN reforms a steadily expanding bubble around the pulsar. It should be noted that this is the ideal case; if the pulsar is not at or near the center of the SNR then the reverse shock front collides asymmetrically with the PWN's expanding shock front and creating a complex 3D system [48].

After the oscillation phase, the pulsar may have travelled beyond its initial expanding shock and forms a new PWN. This is called a "relic PWN" and is characterized by a heavily distorted radio emission morphology with reduced X-ray emission. Generally speaking, IC still occurs at both the pulsar's initial PWN and the newly formed PWN, resulting in a larger TeV gamma ray emission region. As the system ages, IC from the original PWN begins to diminish and the large emission region reduces to a highly asymmetric PWN in the TeV regime [49].

3.4.2 Multi-wavelength emission from PWNe

When the PWN interacts with the ISM, a termination shock front forms and particles can be accelerated to higher energies. Once these particles have been accelerated, they emit radiation in one of two ways: synchrotron radiation and IC. Synchrotron radiation from PWNe is responsible for radio and low energy gamma rays, whose

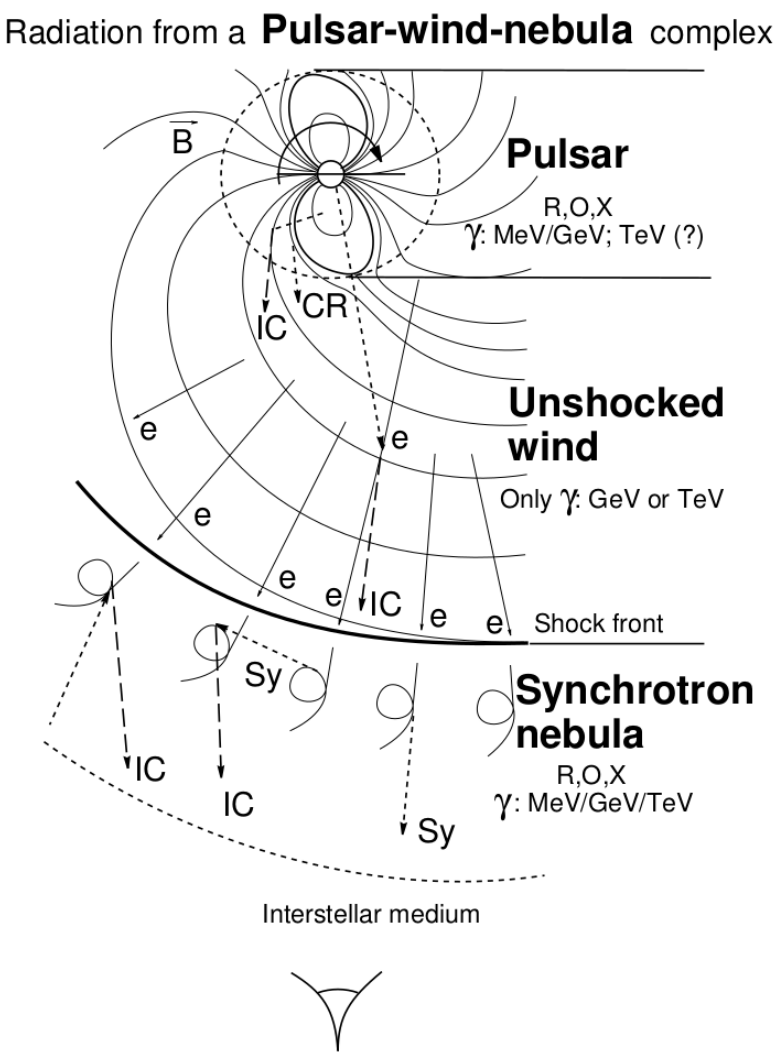

Figure 3.4: Three regions for nonthermal radiation associated with a PWN. The diagram is from [9]

modelling is not considered for this analysis. A discussion of IC can be found in 1.3.2 IC continues the emission from low energy to multi-TeV gamma rays and the different regions where this radiation mechanisms dominate is seen in Figure 3.4.

Due to lower energy requirements, IC emission from a PWN is much larger than that from synchrotron radiation. IC needs low energy photons to produce gamma rays,

and these low energy photons can be found near shock fronts as the PWN transitions to the ISM. This means that IC emission can occur across a large region. The first PWN to be discovered in the TeV regime was the Crab nebula [50] and numerous other PWN have been discovered since. A possible new candidate may be pulsar (PSR) J2032+4127, the hypothesized pulsar powering HAWC J2031+415.

3.5 PSR J2032+4127 and HAWC J2031+415

Gamma ray emission was observed in the Cygnus Cocoon when HEGRA discovered TeV J2032+4130, a TeV gamma ray source with no lower energy counterpart [10]. The excess map can be seen in Figure 3.5. Follow up measurements from Milagro in 200 and 2012 measured small and large extended sources respectfully. The meaning of extended sources will be discuss in Chapter 4 but in short the source extent is correlated to the observed size of gamma ray emission. The 2007 study measured a 0.08° source while the 2012 study found a large 1.8° source [37]. Later in 2014, VERITAS performed a spectral and energy morphological study and they hypothesized that PSR J2032+4127 powered TeV J2032+4130 [12]. PSR J2032+4127 is located at RA=308.04°, DEC=41.46°, where RA (right ascension) and DEC (declination) are defined by the longitudinal and latitudinal lines on Earth. Table 3.1 gives several locations that TeV J2032+4130 has been detected at.

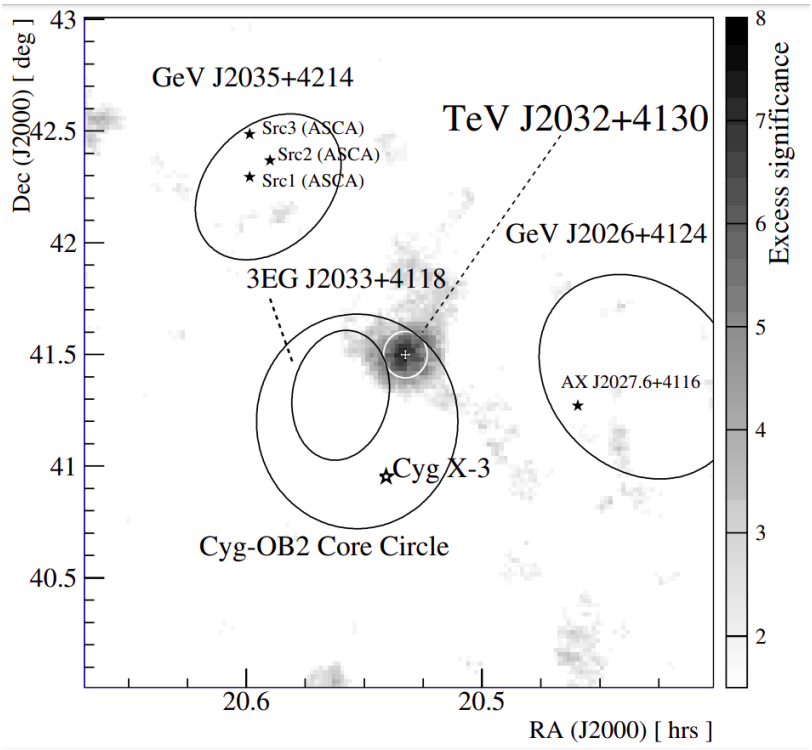

Figure 3.5: First discovery of TeV J2032+4127. Note the Cyg-OB2 region as this will be discussed in Section 5.1. Taken from [10].

Table 3.1
Selected source locations for TeV J2032+4127 prior to this analysis. Source locations are from [12, 13, 14, 15]

Experiment	R.A (in deg)	R.A. Error: Stat(Sys)	Decl (in deg)	Decl Error: Stat(Sys)
HEGRA	307.98	0.1(0.23)	41.49	0.02(0.02)
MAGIC	308.08	0.18(0.18)	41.51	0.02(0.03)
Milagro	307.18	0.42	41.13	0.23
ARGO	308.10	–	41.75	–
VERITAS	307.62	0.02	41.51	0.01
LHAASO	307.98	0.03	41.42	0.03
HAWC (2020)	307.82	0.03	41.51	0.04

Now that the TeV component has been introduced, let us consider the pulsar itself. PSR J2032+4127 was discovered by the Fermi-LAT, a space-based gamma ray telescope, in 2009 as a 143 ms pulsar [51] and has a spin-down luminosity of $\approx 4 * 10^{34}$ erg/s [52]. This pulsar was discovered in close proximity to MT91 213, a V = 11.95 Be star [52]. Be stars are classified as being non-giant phase stars that emit at least one Balmer series line. MT91 213 was estimated to have a mass of $15 \pm 2.8 M_0$ which gives it a relatively short life span of a few million years [53]. Recent observations with Fermi [52] have determined that PSR J2032+4127 and MT 91 213 form a binary pair with an extended orbital period of 50 years. It is believed that, after PSR J2032+4127's parent star went supernova, the kick velocity was not sufficient to escape the gravitational well of MT 91 213, forming this long period system. Additionally, it is a highly elliptical orbit with the orbital velocities ranging from few km/s at apastron (furthermost point) to $>$ 100 km/s at periastron (nearest point) [52].

On the concept of periastron, the binary system was predicted by Fermi to occur in 2017 and this was observed by a joint MAGIC-VERITAS collaboration. The joint observations confirmed the binary nature of PSR J2032+4127 but note that the measured size and luminosity of the TeV gamma ray emission is significantly smaller than predicted. Given the complex nature of the binary pair and, combined with the large eccentricity and orbital period, PSR J2032+4127 may yet be the power source for TeV J2032+4130 [54]. In this work I investigate this claim with HAWC.

Chapter 4

Analysis Methodology

This chapter will discuss the analysis method that a HAWC analysis goes through and how a final model is determined. Additionally a new systematic source search method is introduced in Section 4.4.

4.1 Likelihood Method

The core framework that HAWC utilizes to analyze high-level data like gamma ray sky maps is the Multi-Mission Maximum Likelihood framework (3ML) and the full framework is discussed further in [55]. The likelihood analysis technique determines the probability of observed data $x_i, ..., x_n$ given the probability function $P(x_i, ...x_n; \vec{\theta})$

given by [56].

$$L(\vec{\theta}|x_1, ..., x_n) = \prod_{i=1}^{n} P(x_i|\vec{\theta}) \tag{4.1}$$

The maximum likelihood method determines the parameters $\vec{\theta}$ that maximizes the probability of the data given the model. The data is then reconstructed events using the 3 energy estimators that HAWC uses: f_{hit}, ρ_{40}, and a neural network, and are discussed further in Section 4.3. The next step is to construct a model that will be fitted to the data.

4.1.1 Model Parameters

A HAWC analysis fits both the morphology (emission shape in the sky maps) and the spectra of gamma ray sources. There are two morphologies considered: a point-like source and an extended source. The morphology is considered "point-like" or point source if the extension of the source is equal to or smaller than HAWC's angular resolution. HAWC's angular resolution is a function of energy and ranges from $> 0.1°$ for > 56 TeV to $> 1°$for $\approx$ 1TeV high energy events and may not be a point source for other arrays. There are several models available in 3ML and three relevant ones for this analysis are disk, symmetric Gaussian, diffuse background emission (DBE)

models. The DBE model handles both galactic background emission and emission from unresolved sources in a given Region of Interest (ROI). The spectral component of these models is initially discussed and then morphology functions are discussed afterwards.

All morphologies (point-like and extended sources) have a spectral component as well and the relevant models are introduced here. The simplest is a basic normalized power law spectrum shown given by

$$\frac{dN}{dE} = N_o \frac{E}{E_p}^{-\alpha}, \tag{4.2}$$

Where N_o is the flux normalization, E_p is the pivot energy, and α is the spectral index. The pivot energy is used to de-correlate the flux normalization and index, forcing the correlation between the two to zero. E_p has no impact on the numerical value of the fitting results.

Another spectral model considered is the power law with an exponential cutoff:

$$\frac{dN}{dE} = N_o \frac{E}{E_p}^{-\alpha} \exp \frac{E}{E_c}. \tag{4.3}$$

The additional parameter E_c is the cutoff parameter and determines how quickly the

spectrum decays with increasing energy.

The last model considered in this analysis is the log-parabola model, given by

$$\frac{dN}{dE} = N_o \frac{E}{E_p}^{-\alpha-\beta \ln E/E_p}. \tag{4.4}$$

The log-parabola model is characterized as being a parabola in log-log space where β is the curvature parameter. One characteristic of HAWC is using a multi-source fitting process, meaning there can be multiple source models added to the ROI and all freed parameters are fitted simultaneously.

Now a discussion on the morphologies available for these sources. A point source is treated as an extend source that has a fixed width and is the smallest source HAWC can resolve. This width is a function of the resolution of the detector and reconstructed data. For the 2D Gaussian model, the flux normalization is modelled as a Gaussian and tapers off the further from the source center. The expression for this model is given as [57]

$$f(\vec{x}) = (\frac{180^\circ}{\pi})^2 \frac{1}{2\pi\sqrt{\det \Sigma}} \exp\left(-\frac{1}{2}(\vec{x} - \vec{x_o})^\intercal \Sigma^{-1} (\vec{x} - \vec{x_o}\right), \tag{4.5}$$

Where $\vec{x_o}$ is the (RA_o, Dec_o) and Σ is the covariance matrix such that, for Λ and U

$$\Lambda = \begin{pmatrix} \sigma^2 & 0 \\ 0 & \sigma^2(1-e^2) \end{pmatrix}$$

$$U = \begin{pmatrix} \cos\theta & -\sin\theta \\ \sin\theta & \cos\theta \end{pmatrix}$$

the covariance matrix is $\Sigma = U\Lambda U^{\intercal}$ where σ is the standard deviation of the Gaussian and e is the eccentricity of the Gaussian (for symmetric models $e = 0$).

For a disk model, the flux normalization is held constant across the desired radius r and is zero elsewhere:

$$f(\vec{x}) = (\frac{180^\circ}{\pi})^2 \frac{1}{\pi(\text{radius})^2} \begin{cases} 1 & \text{if } |\vec{x} - \vec{x_o}| \leq \text{radius} \\ 0 & \text{if } |\vec{x} - \vec{x_o}| > \text{radius} \end{cases}. \tag{4.6}$$

The last model discussed in this thesis is the DBE model and is given by

$$f(\vec{x}) = K \exp \frac{-b^2}{2\sigma_b^2}, \tag{4.7}$$

where K is a normalization factor, b is the galactic longitude range being considered, and σ_b is the radius of the model along the galactic plane. The radius was determined

by a galactic diffuse emission study by the High Energy Stereoscopic System (HESS) and determined the radius to be 1° [58].

4.1.2 Fitting the Model

Once the model has been constructed, it is time to fit the model to the data. The observed events in each pixel of data is given by the Poisson distribution shown as

$$P_i = \frac{\theta_i^{n_i} e^{-\theta_i}}{n_i!}, \tag{4.8}$$

where n_i is the number of observed events in a pixel and θ_i is the expected number of events given the assumed galactic background. The likelihood L is the product of probabilities of observing the number of detected events

$$L = \prod_{i=1}^{N} P_i, \tag{4.9}$$

The log of the likelihood function below is considered.

$$\log L = \sum n_i \log \theta_i - \sum \theta_i - \sum \log n_i! \tag{4.10}$$

The final model is what combination of θ_i parameter values minimizes the negative log(likelihood).

4.2 Model Comparison

Once a fit has been completed with a certain model, the next step is to compare that fit result to a new model and determine which better represents the emission observed. This is done by a likelihood ratio test [55]

$$TS = 2 \ln \frac{L_{alt}}{L_{null}}, \tag{4.11}$$

where L_{alt} is the alternate hypothesis, typically the model used for observed gamma ray emission, and L_{null} is generally the background-only model. This approach is based on Wilks' Theorem and, for nested models, the TS distribution follows a χ^2 distribution with degrees of freedom equal to the number of free parameters [59]. For one free parameter, the significance is given by

$$\sigma = \sqrt{TS}. \tag{4.12}$$

It should be noted that σ in this context is the significance of a parameter, not the width of a Gaussian as used in Section 4.1. This σ parameter is relevant to the data maps that HAWC generates as the model parameter difference is 1: the background only assumption and a source + background with the flux normalization being fit. Previous studies with HAWC have determined that a $> 5\sigma$ indicates a source present in the significance map. Examples of these maps will be shown in Chapter 5.

4.2.1 ΔTS comparison

Models can be compared by considering the difference in TS or ΔTS between them. Consider 2 models, one with Equation 4.2's spectral model and the other using Equation 4.3's. The ΔTS of the two models is found and, given that the -log(likelihood) is found in the fitting process, the final result is given by

$$\Delta TS = 2(\log(\text{Model 1}) - \log(\text{Model 2})). \tag{4.13}$$

If $\Delta TS < 16$, then the simpler model is preferred. It should be noted that a ΔTS value of 16 is an a priori threshold for model comparison. The HAWC group at Michigan Technological University is currently performing studies to verify the corresponding probability value. Based off current results, 16 is currently believed to be

Table 4.1
ΔBIC comparison [16]

ΔBIC	Evidence against higher BIC model
0 to 2	no evidence
2 to 6	Positive
6 to 10	strong
>10	very strong

the optimum value.

4.2.2 Bayesian Information Criterion

Another metric, the Bayesian Information Criterion (BIC), can be used to confirm the ΔTS result. It is defined as

$$BIC = -\log L - k \log n, \tag{4.14}$$

where k is the number of free parameters, n is the data set size, and the $-\log L$ term is the usual log(likelihood) function. The additional term $k \log n$ term serves as a penalty for models involving more parameters. It should be noted that BIC comparison is not valid when k and n are comparable. The meaning of different ΔBIC values is given in Table 4.1 [16].

4.3 Map files

Now that the model is constructed and they can adequately be compared, now we need the data sets to model. HAWC uses three energy estimators: Fractional Hit (f_{hit}), Neural Network (NN), and Ground parameter (GP) or ρ_{40} and each will be discussed here.

4.3.1 Fractional Hit

The f_{hit} array is the first and most basic energy estimator. It functions by binning the events into separate bins depending on how much of the array was triggered by an EAS. Each bin consists of a percentage range of the array triggered and the data set is divided into eleven bins. The f_{hit} binning scheme can be seen in Table 4.2. This estimator stores hits and can be used to perform analyzes but is inadequate for energy reconstruction as a >10 TeV event will trigger the entire array.

4.3.2 Neural Network Estimator

The NN estimator uses the Toolkit for Multivariate Analysis neural network implementation [60]. There are 3 characteristics of the EAS that are chosen: the energy

Table 4.2
Pass 5 f_{hit} binning scheme

Bin	Low fraction hit	High fraction hit
0	0.027	0.047
1	0.047	0.07
2	0.07	0.11
3	0.11	0.16
4	0.16	0.25
5	0.25	0.37
6	0.37	0.51
7	0.51	0.66
8	0.66	0.78
9	0.78	0.88
10	0.88	1.0

amount saturating the detector, the extent that the shower footprint is contained by the array, and the degree of attenuation of the shower from the atmosphere. A more in-depth discussion for the NN implementation can be found in [38]. Due to the increase in energy sensitivity due do the reconstruction process, both the NN and ρ_{40} can sub-divide each f_{hit} bin into 12 sub-bins. The energy range for each sub-bin can be seen in Table 4.3. The binning syntax is as follows: for bin 0 sub-bin a the name for pass 5 data bins is B0C0Ea where C0 indicates on-array (directly impacts the HAWC array) event.

Table 4.3
Quarter decade energy bins for ρ_{40} and NN maps

Bin	Energy Range (TeV)
a	0.316 - 0.562
b	0.562 - 1.0
c	1.0 - 1.78
d	1.78 - 3.16
e	3.16 - 5.62
f	5.62 - 10.0
g	10.0 - 17.8
h	17.8 - 31.6
i	31.6 - 56.2
j	56.2 - 100
k	100 - 177
l	177 - 316

4.3.3 ρ_{40} Estimator

The ρ_{40} estimator (also referred to as "ground parameter" in published HAWC analyzes) functions by estimating the charge density at a fixed optimal distance from the shower core. The global estimate for the optimum radius was determined to be 40 meters and a further discussion for the derivation of this value can be found in [38]. The charge density can be related to the gamma ray energy by

$$\log_{10} E = m(\theta) \log_{10} \rho_{40} + c(\theta), \tag{4.15}$$

where $m(\theta)$ and $c(\theta)$ are linear and quadratic piecewise functions with respect to the

zenith angle and ρ_{40} is the charge density at 40 meters. All three estimators are used in this analysis and is discussed further in Chapter 5.

4.4 Systematic Source Search

The final step to analyze an emission region is to determine how many sources are present, what their morphologies are, and what spectral model each source has. Previous studies proceeded with a non-robust search method to determine the best model selection but for this study a systematic approach is taken. The method is a variation of a source search method performed by the Fermi LAT collaboration and is discussed in detail in [61]. The key difference between Fermi's method and this study is in the method that sources are added to the ROI.

The first step is to model the diffuse background emission (DBE) that handles both background and emission from unresolved sources. Once fitted, a point source (PS) is added near the highest residual significance and has the location and spectral components fitted. After a PS is added to the ROI and fitted, the next step is to determine which model is preferred, the one with the additional PS or without it. For this study, a ΔTS of 16 or greater results in the additional PS to be kept in the model. Additionally, if the individual TS of any source drops below 16, they are excluded from the model. This is due to the possibility of the PS being a high

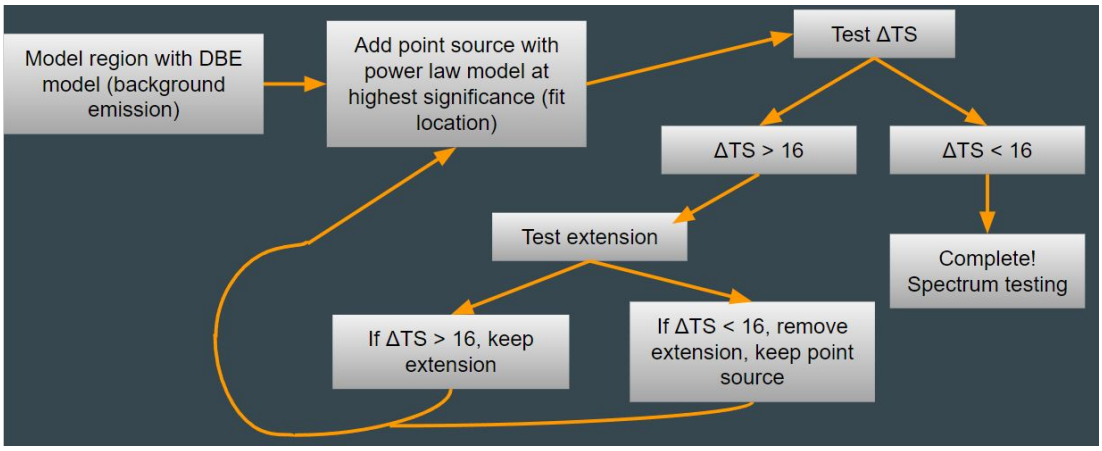

Figure 4.1: Systematic source study.

fluctuation in the background data set. If the PS model is preferred, then the next step is to test the extension of the source.

The extension test is as follows: the added PS is made into an extended source (2D symmetric Gaussian) and the fit is re-done. If the ΔTS is greater than 16, the extension is kept. It should be noted that during this process the source location remains free as the best fit location of an extended source may differ from a PS. If $\Delta TS < 16$, then the extension test is rejected and the source is kept as a point source. Then a new PS is added at the next highest residual significance and the process repeats. The study is concluded when the ΔTS from adding a new PS is less than 16, then the final source model has been found. This process is shown in 4.1.

Once the number of sources has been identified, the next step is to determine the spectrum of each source. This is done by taking one source and performing three fits, one for each spectrum discussed in Section 4.1.1. As an additional checks, BIC is

used in addition to ΔTS. The threshold for a preferred model is given by $\Delta TS > 16$ or $\Delta BIC > 2$. Once that source's spectrum has been identified, it is kept in the model and the test proceeds to the next source. In the case of a tie in BIC or ΔTS between models, the simpler model is preferred. One additional check that can be done is to observe a 1D significance histogram of the data distribution. If there is only background emission and no source, the expected outcome of the histogram is a Gaussian shape with a mean of 0 and a width of 1. This study is done using the f_{hit} estimator and a selection of steps is given in Chapter 5.

Chapter 5

HAWC Analysis of HAWC J2031+415

This chapter will discuss the systematic source search results with all three estimators as well as the spectral fitting results of these sources. Additionally I will also discuss the energy morphology study of HAWC J2031+415 with the ρ_{40} and NN estimators.

5.1 Sources Considered

The data maps considered for each estimator are as follows: for f_{hit} the bins used are B2C0 B3C0 B4C0 B5C0 B6C0 B7C0 B8C0 B9C0 B10C0, where the C0 indicates

on-array hits and the NN and ρ_{40} bin lists can be found in Appendices B and C respectfully. These bins are selected based on 2 key requirements: having a Point Spread Function (PSF) fit of less than one degree and having data at a declination of 40 degrees. The PSF is related to the extent that a PS can be resolved with the HAWC detector and is discussed in more detail later. An example for the f_{hit} estimator and the ROI considered for this analysis can be seen in Figure 5.1. The additional initial data maps for ρ_{40} and NN are found in C and B respectfully.

The ROI used has a mask on 3HWC J2019+367, the brightest source in the Cygnus region to HAWC, to prevent potential bleed-over emission that could affect results. Additionally, previous work with HAWC [14, 15] has observed a large extended source with width greater than two degrees, so the ROI needs to be large enough to ensure no emission is lost. The modified systematic source search method is applied to these three maps with this ROI.

5.1.1 Systematic Source Search Results

The f_{hit} map was used for the systematic source search method. The initial map is seen in Figure 5.1. The first step is to fit the DBE model and examine the results. The results from this fit can be seen in Figure 5.2.

Now that this model has been fit, the extension test is applied. The relevant plots

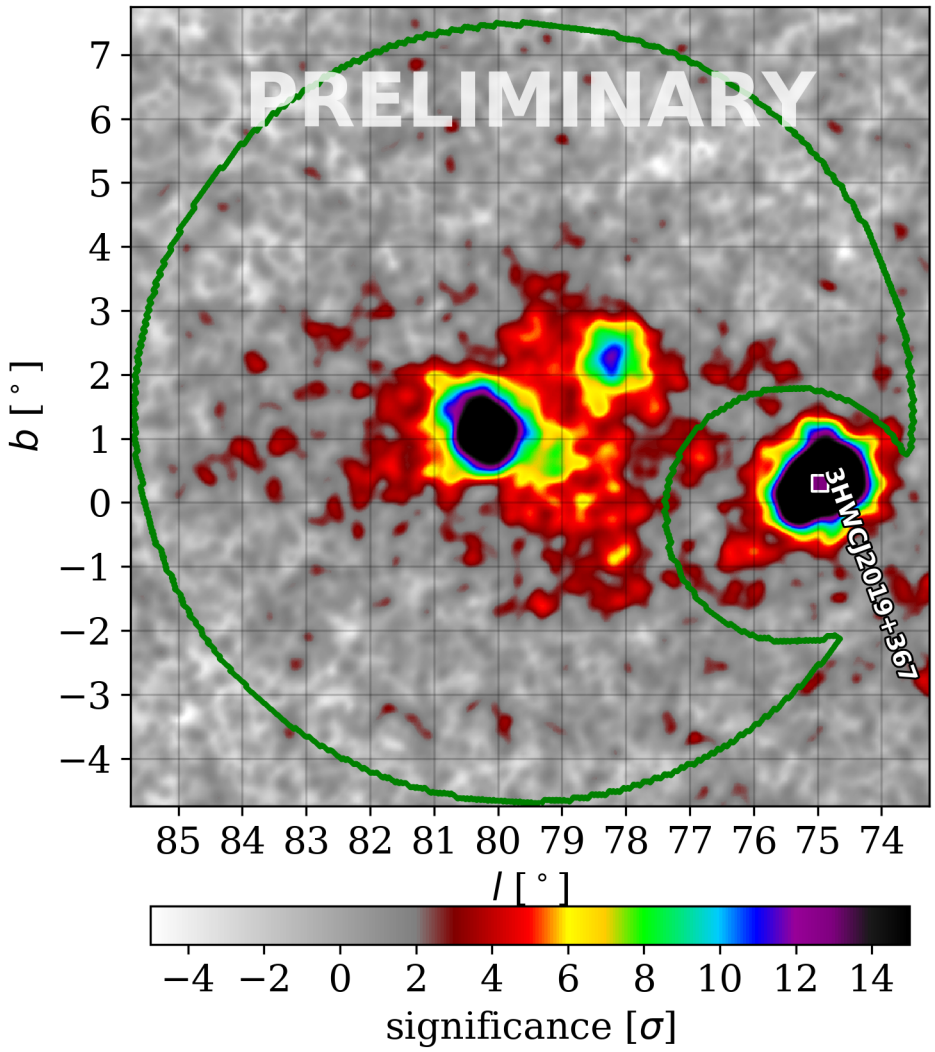

Figure 5.1: The f_{hit} map. The coordinates are given as galactic longitude l (distance from the galactic center) and galactic declination b (distance from galactic plane).

for each step can be found in Appendix A while the final model can be seen in Figure 5.3.

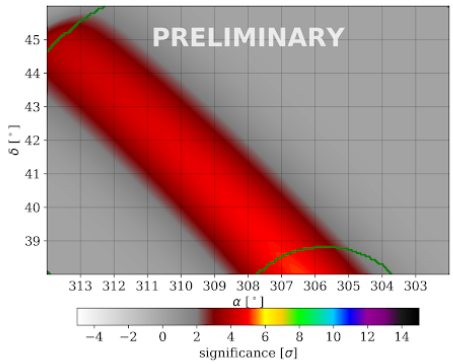

(a) DBE only model significance map.

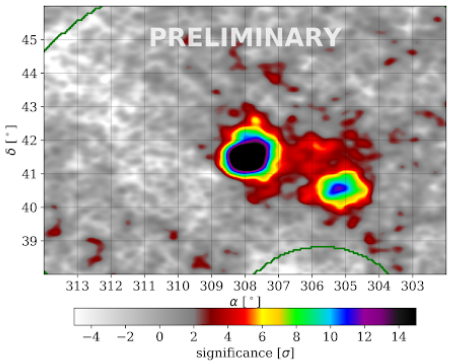

(b) The residual map after subtraction of the best fit DBE model.

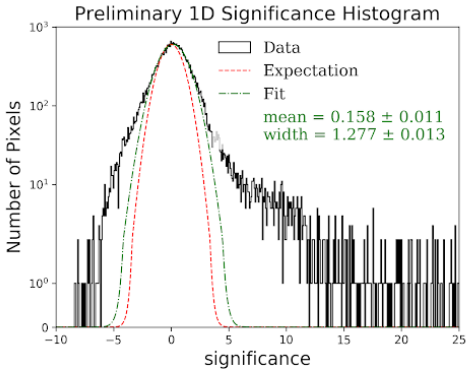

(c) The residual 1D histogram after subtraction of the best fit DBE model.

Figure 5.2: Results of DBE only model. Figure 5.2(a) has been smoothed with a 0.5 degree extension to more easily observe extended sources. Figure 5.2(b) is made with a point source assumption (no additional smoothing applied). The 1D histogram of the residual data map is shown in Figure 5.2(c). As the fitting process proceeds, the histogram trends towards a normal Gaussian shape.

One note is the remaining negative shoulder in the adjusted 1D histogram in Figure 5.3(c). This is present in all current HAWC pass 5 data maps. This is believed to be an artifact of new background calculations and is still being investigated. It has been verified that it does not affect the fit results. Additionally the negative excess

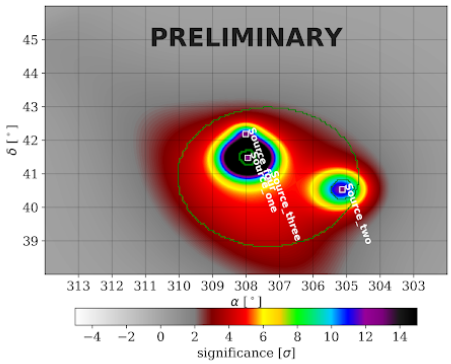

(a) Final model significance map.

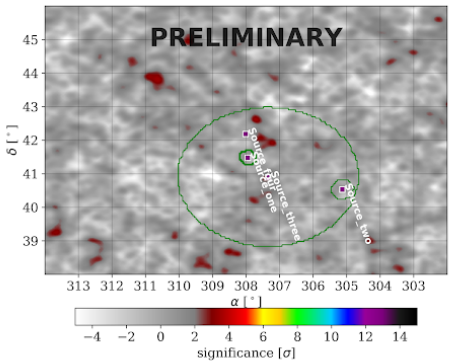

(b) The residual map after subtraction of the best fit model.

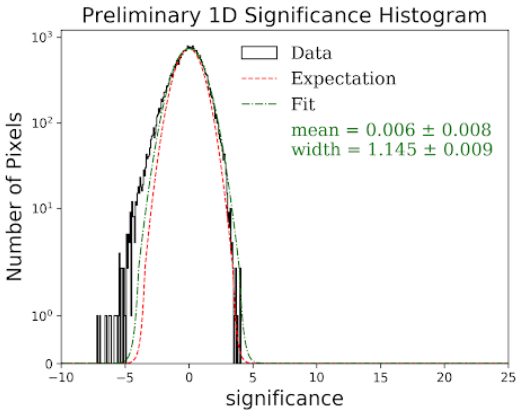

(c) The residual 1D histogram after subtraction of the best fit model.

Figure 5.3: Results of the final model. The green contours in both Figures 5.3(a) and 5.3(b) indicate the extent of each extended source. The new source location would be at (307.72 42.61) with a significance of 3.44. The next step, DBE + 3 EXT + 2 PS had a $\Delta TS = 2$ and was rejected.

past -5 in Figure 5.3(c) is caused by a small discrepancy from data to model where the model has emission but the data map does not. This is not considered in this analysis but more work is needed to resolve this discrepancy.

The final model results for the f_{hit} modified extension systematic study method is

Table 5.1
f_{hit} sources and extensions

Source	R.A (∘)	Decl (∘)	Extension (∘)	TS
Source 1	307.95 ± 0.05	41.48 ± 0.01	0.21 ± 0.01	130.17
Source 2	305.13 ± 0.06	40.53 ± 0.04	0.28 ± 0.04	120.79
Source 3	307.34 ± 0.02	40.90 ± 0.17	2.06 ± 0.12	130.15
Source 4	308.01 ± 0.05	42.19 ± 0.02	–	23.27

given Table 5.1.

Sources 1, 2, and 3 all correspond to observed HAWC sources [14, 15] but source 4 is a newly discovered source with no association in TeVCat[1], a data base that collects information on astrophysical sources. It should be noted that it is standard practice for HAWC to require a source to have a TS of greater than 25 for new sources. Source 4 is kept as it passes the TS=16 requirement from the source search study but further studies and additional are required to determine whether source four is a new source or a background fluctuation in the f_{hit} data map. For this analysis it is kept as it passed the source study criteria while for NN and ρ_{40} source four's TS$<$ 16 and was dropped.

Once the number of sources has been determined, next comes the morphology and spectrum curvature tests. In previous works [14, 15], not all sources in the ROI were symmetric Gaussians. In particular, source two was modelled as a disk (see Section 4.1.1) with a fixed radius of 0.63°. There was no significant ΔTS meaning the simpler

[1] `http://tevcat.uchicago.edu/`

disk model was preferred over the Gaussian model (one less free parameter). The other two extended sources preferred symmetric Gaussians to disk models.

For the curvature tests, both ΔTS and ΔBIC are considered. The model with the smallest ΔBIC is taken unless $\Delta BIC \leq 2$, in which case the simpler model is taken. A curvature study could not be completed for source four as its low significance hindered fits from converging. Tables 5.2 5.3, and 5.4 show the preferred spectral models for sources one, two, and three respectively.

Table 5.2
f_{hit} Curvature test for Source 1. The preferred model for source 1 is a power law with an exponential cutoff.

Model	-log(likelihood	ΔBIC
4 PL	136145	272519
3 PL 1 LP	136111	272384
3 PL 1 PLC	136109	272381

Table 5.3
f_{hit} Curvature test for source 2. The preferred model for source 2 is a power law.

Model	-log(likelihood	ΔBIC
1 PLC, 3 PL	136109	272381
1 PLC, 2 PL, 1 LP	136109	272392
1 PLC, 2 PL, 1 PLC	136109	272393

Once the study is concluded, the astrophysical objects associated with each source are considered. Source one's location correlates to HAWC J2031+415, source two's location is coincident with the SNR Gamma Cygni, source three is associated with

Table 5.4
f_{hit} Curvature test for source 3. The preferred model for source 3 is a log parabola.

Model	-log(likelihood	ΔBIC
1 PLC, 3 PL	136109	272381
1 PLC, 2 PL, 1 LP	136093	272362
1 PLC, 2 PL, 1 PLC	136095	272365

the Fermi-LAT Cocoon, and source four has no currently known counterpart. The curvature and location tests for the NN and ρ_{40} maps returned the same results as the f_{hit} estimator and all three are shown in Table 5.5. The pivot energy E_o for sources one, two, and three are set to 4.9, 1.1, and 4.2 TeV respectively from [62].

5.2 Isolating the PWN

Now that a model has been found, it is time to isolate the source of interest HAWC J2031+415. To disentangle J2031+415, the other sources are fixed to their best fit values and are subtracted out of the ROI. Due to the lack of sensitivity above 10 TeV, only the ρ_{40} and NN data maps will be considered hence forth. The model (excluding the PWN contribution) and the data map after subtraction are shown in Figure 5.4.

Table 5.5

f_{hit}, NN, and ρ_{40} spectrum fit results. The curvature parameter represents either the cut-off energy or the beta term in the log parabola model. The units are indicated where necessary. Not included is the DBE model, though it was present in all three estimator models. It is dropped from the table because its ΔTS was 16 with the final models.

Estimator	Source	Width ∘	Flux (TeV/cm^{2}s)	Index	Curvature	TS
f_{hit}	J2031+415	0.22 ± 0.02	$(1.12 \pm 0.12)10^{-13}$	-1.97 ± 0.13	32 ± 6 TeV	817.57
	Gamma Cygni	0.63 (fixed)	$(44 \pm 11)10^{-13}$	-3.02 ± 0.10	—	125.64
	Cocoon	2.03 ± 0.13	$(2.2^{+1.6}_{-0.3})10^{-13}$	-2.74 ± 0.05	0.143 ± 0.032	228.04
	J2032+422	—	$(3.5^{+1.3}_{-0.9})10^{-15}$	-2.72 ± 0.18	—	23.14
NN	J2031+415	0.25 ± 0.02	$(1.33^{+0.20}_{-0.17})10^{-13}$	-1.9 ± 0.6	24^{29}_{13} TeV	476.88
	Gamma Cygni	0.63 (fixed)	$(40^{+7}_{-6})10^{-13}$	-2.93 ± 0.08	—	81.99
	Cocoon	2.13 ± 0.16	$(2.70^{+0.32}_{-0.28})10^{-13}$	-2.76 ± 0.05	0.117 ± 0.031	180.61
ρ_{40}	J2031+415	0.26 ± 0.02	$(1.57^{+0.15}_{-0.13})10^{-13}$	-1.8 ± 0.6	20^{+20}_{-10} TeV	417.00
	Gamma Cygni	0.63 (fixed)	$(35^{+6}_{-5})10^{-13}$	-2.82 ± 0.07	—	94.90
	Cocoon	2.17 ± 0.13	$(3.30^{+0.31}_{-0.28})10^{-13}$	2.72 ± 0.06	0.22 ± 0.04	186.03

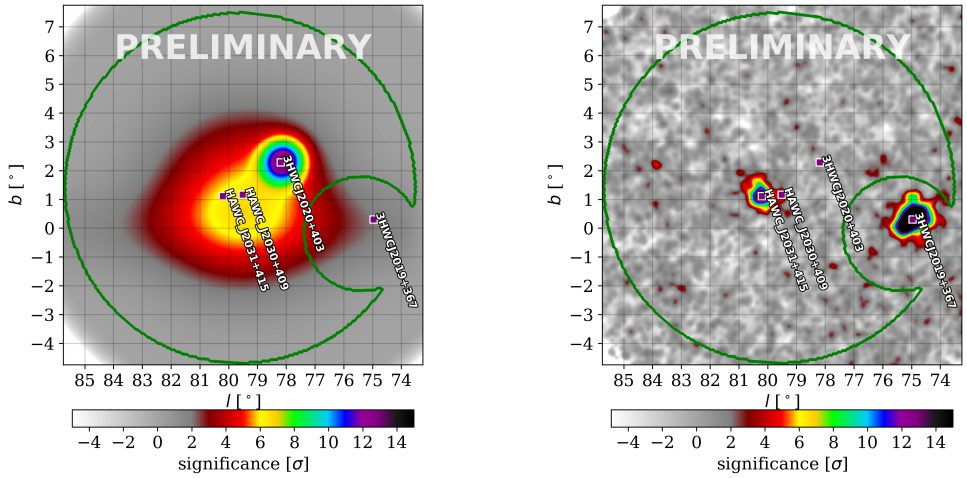

(a) Model significance map without PWN.

(b) Residual significance map.

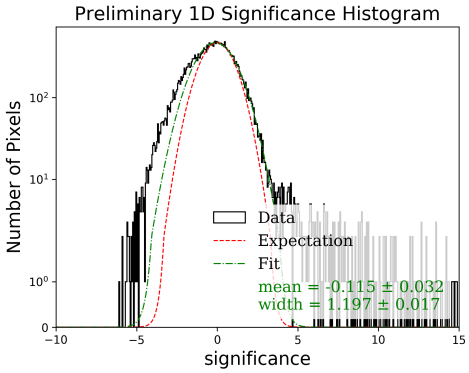

(c) Residual 1D histogram.

Figure 5.4: The isolating process for the ρ_{40} data map. Figure 5.4(a) is made with a 0.5° extension to properly show the $> 2°$ extent of the Cocoon. Figure 5.4(b) is made with a PS assumption.

Once J2031+415 has been isolated, two additional studies are performed to test the PWN assumption. The first is to confirm the best fit spectral model (power law with exponential cut-off) and this is shown in Figure 5.5. The second study is an energy

morphology study and is discussed in Section 5.3.

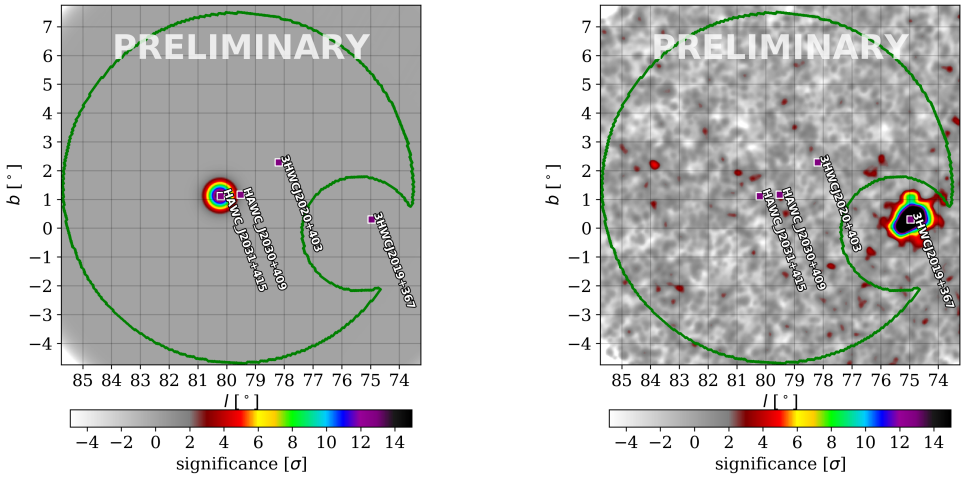

(a) Model significance map of PWN.

(b) Residual significance map.

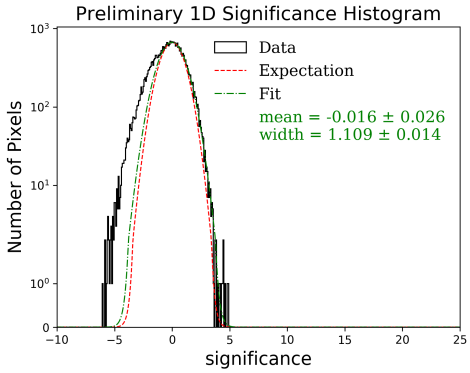

(c) Residual 1D histogram.

Figure 5.5: The final result after the PWN is subtracted. This uses the proper model for the PWN (power law with exponential cut-off) and the residual data map shown in Figure 5.4(b)

5.2.1 Energy Limits

To determine the energy range over which the spectrum is measured for each source, a study similar to the one in [63] is done for all three sources in both the NN and ρ_{40} data maps. The lower and upper thresholds of the energy spectra are determined by multiplying each spectral model (power law, log parabola, and power law with exponential cut-off) by a step function that models an abrupt spectral cutoff. The only free parameters are the upper and lower cut-off values, all other parameters are fixed at their best fit values. These energy boundaries are varied until the fit significance drops by 1 σ. Where the -log(likelihood) crosses the 1σ threshold of the upper energy cut-off, the lower limit to the gamma ray energy is found. Likewise, when the -log(likelihood) crosses the 1σ for he lower energy cut-off, the upper limit for the minimum gamma ray energy detected is found. The results for the ρ_{40} data map can be seen in Figure 5.6 while the NN results can be found in Appendix B.

Table 5.6
NN 1σ energy limits in TeV units

Source	Lower Limit	Upper Limit
J2031+415	0.7	76
Cocoon	0.5	127
Gamma Cygni	0	77

With these energy limits accounted for, the spectrum of each source can be properly interpreted. The energy ranges for each source is given in Table 5.6. The spectrum

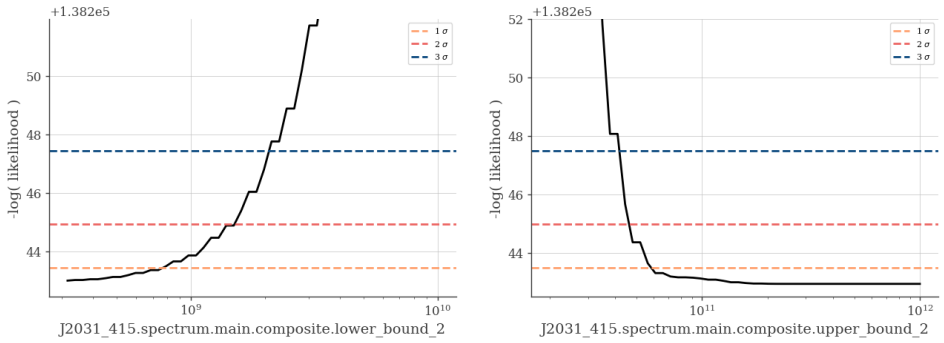

(a) J2031+415 lower bound.

(b) J2031+415 upper bound

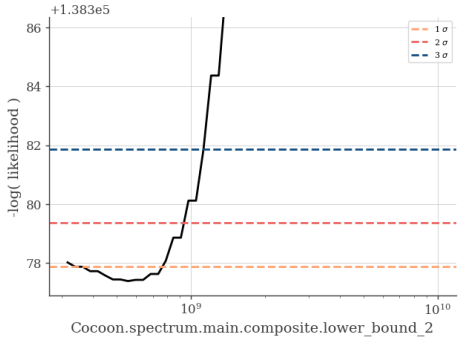

(c) Cocoon lower bound

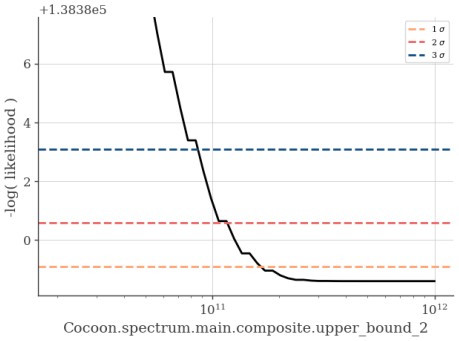

(d) Cocoon upper bound

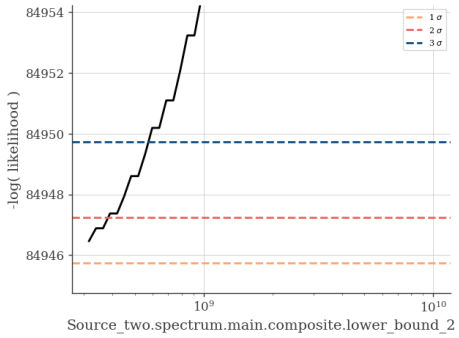

(e) Gamma Cygni lower bound

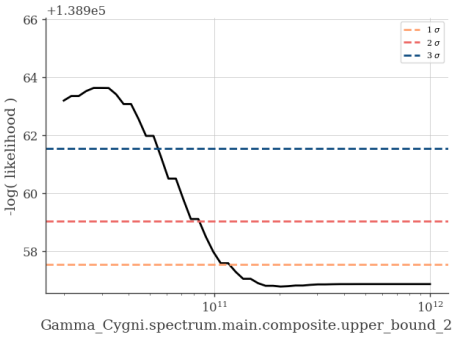

(f) Gamma Cygni upper bound

Figure 5.6: The energy range study of the three sources using the ρ_{40} data map. The NN study is shown in Appendix B. The dashed lines represent the 1, 2, and 3 σ thresholds. Figure 5.6(e) has no 1 σ due to a divide by zero error encountered when 0 TeV was selected. Its 2 σ is selected for its lower energy bound.

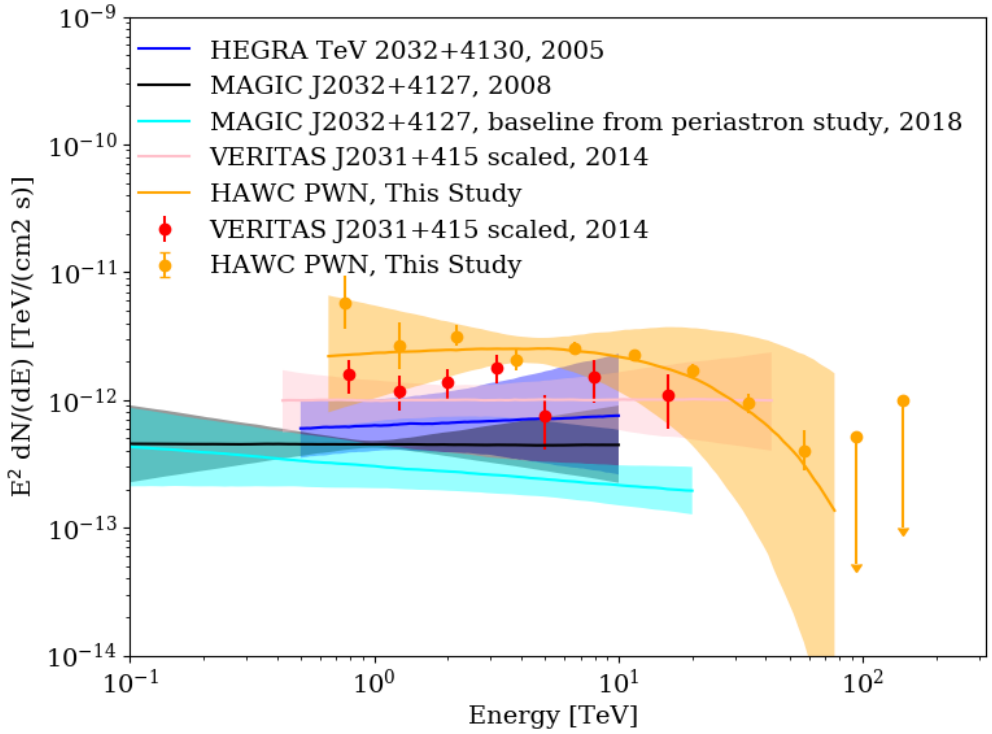

Figure 5.7: The spectrum of HAWC J2031+415 compared with selected observations. The VERITAS observation is scaled due to the difference integration angles and is scaled with a factor of 1.49 (see [11] for more details). Additionally, the upper limits belong to energy bins k and l, and occur outside of the determined 1σ energy ranges.

and flux points of J2031+415 are shown in Figure 5.7. The flux points are calculated after the fitting process and fix each parameter to their best fit values except for the flux. Then each energy bin group (a, b, etc) are collected and the flux is fitted to that data map. The flux calculation is independent of the other sources; i.e., it is calculated for one source at a time.

5.3 Energy Morphology Study of HAWC J2031+415

This section will explore the energy morphology of HAWC J2031+415. To do this, a slicing profile tool described below is utilized and the isolated PWN data map is used. Additionally, this data is separated into discrete energy bands

5.3.1 Slicing Profile Tool

Performing direct fits in each band may not result in well constrained fits, especially around the cut-off point (≈ 20 TeV). Therefore an alternative method is used. Similar to the energy morphology studies done by VERITAS [5], a tool was designed by Vikas Joshi, a fellow HAWC member, that allows such a study to be completed [22]. An example of this tool being used on the Crab Nebula (henceforth Crab) can be seen in Figure 5.8.

The tool functions by first slicing a region into a rectangle. The dimensions and angle of this rectangle are user defined and, unless otherwise specified, are a 6x1 degree large region rotated 16.7°. The rotational angle was determined from the positions of HAWC J2031+415 and PSR J2032+4127. For point sources the rotational angle

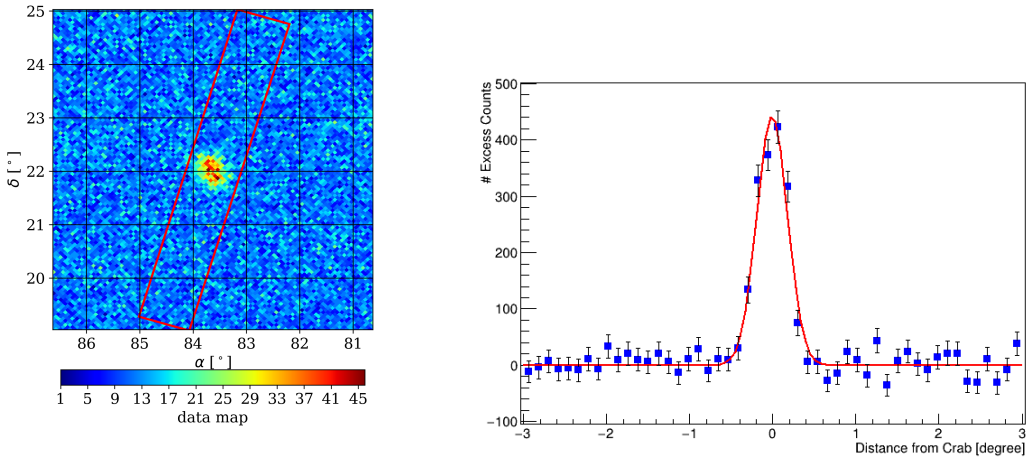

(a) (b)

Figure 5.8: Example of the slicing profile tool. The left figure shows the counts (or event number) map where the red rectangle represents the region selected for the slicing analysis. The excess count profile in this bin can be see on the right where a 1D Gaussian is fitted to the data. The plotted bin is B6C0Ef

is irrelevant but for extended sources the angle can determine whether emission is missed or not.

With this rectangle defined, it is then sliced into rectangular sub-bins (henceforth bins) that are summed to create the excess count profile shown in Figure 5.8(b). For this analysis 50 bins are used, each with a width of 0.12°. It should be noted that, for the maps shown in this analysis, the pixel width is 0.05° and the bin size should be significantly greater than that to prevent slicing each pixel. Lastly, for point sources the Gaussian fitted to the excess count profile can be treated as an analog to PSF and is denoted as PSF'. As a reminder, PSF is the smallest source that HAWC can resolve in a 3ML fit while the point source PSF' is the smallest source the excess

count profile can resolve. These two values are not the same but follow the same trend (larger for lower energy bins, smaller for higher energy). This effect will be accounted for in Equation 5.2 in Section 5.3.4.

5.3.2 Systematic Studies

Theoretically, the slicing tool could be used on every bin used in the initial fit. However, there are two key factors preventing this:

- The PSF quality of each bin varies greatly with the shower size.
- Not all bins contribute equally to a source's significance.

To perform a morphology study, the best possible PSF is required without significantly reducing the available data. Therefore, studies must be done to remove bins that detract from this PSF. To do this, a bright source, like the Crab, is needed. However, HAWC's PSF changes with declination and, given that the Crab's declination is at 22° and J2031+415 is at 41.5°, simulations must be done to determine the proper bins at J2031+415's declination. This study can be split into two focuses:

- Check the consistency of data vs simulation at different declinations.
- Verify the bin selection is valid at different declinations.

5.3.2.1 Data and Simulation Comparison

To test the consistency of the PSF at different declinations, 2 bright points source, Crab and Markerian 421 (Mrk 421) are considered. Crab is selected because it is the brightest source visible to HAWC ($> 150\sigma$) and passes almost directly overhead the array and Mrk 421 is used because it is a bright source ($\approx 80\sigma$) near J2031+415's declination at 38°. To simulate these sources, both are fit with a simple power law model and then simulated at their respective positions. This study is done with both NN and ρ_{40} maps. The NN maps are shown below in Figure 5.9 and the ρ_{40} are shown in Appendix C.

In addition to the PSF' of data and simulation comparison, there is also a normalized plot that is used to show any systematic difference between the two. This plot used the normalization factor given by

$$\frac{\text{Data} - \text{Sim}}{\sqrt{\text{Sim}}}. \tag{5.1}$$

If the PSF' distribution is centered around 0, then there is no systematic offset. However, if it deviates then there is a systematic offset that must be accounted for in the final morphology result.

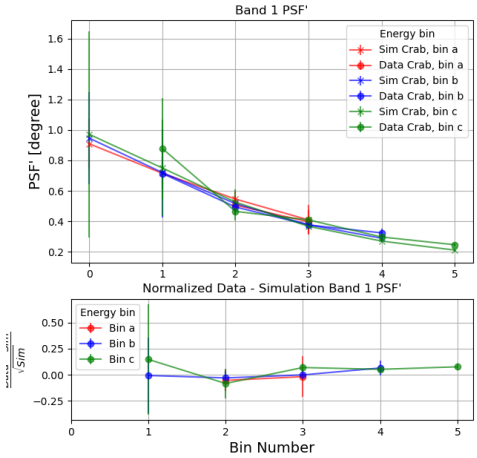

(a) First band.

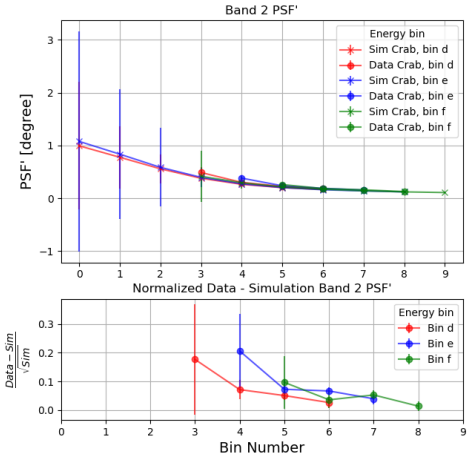

(b) Second band.

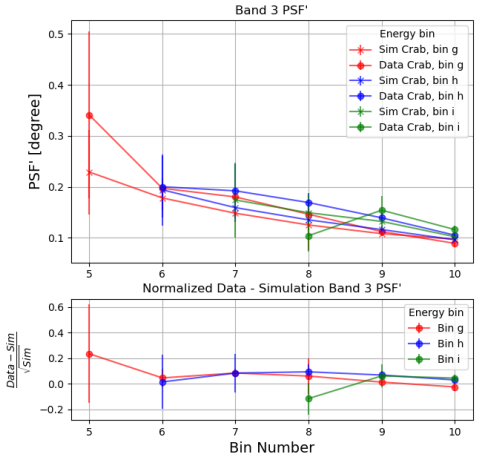

(c) Third band

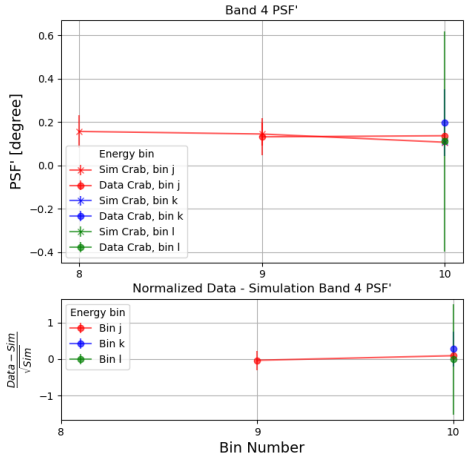

(d) Fourth band.

Figure 5.9: The PSF' as a function of NN bins. Each plot has three of the decade bins a-l and in the top plot the comparison between data and simulated PSF' is shown. Note that not all data bins have a PSF' as not all bins have enough data to perform a fit, even with the Crab. The lower plot is the normalized difference between data and simulation to determine if there is a systematic difference between data and simulation.

It can be seen from Figure 5.9 that there is a systematic difference between data and simulation. This is graphically seen in Figure 5.10. The large uncertainty in band 4's

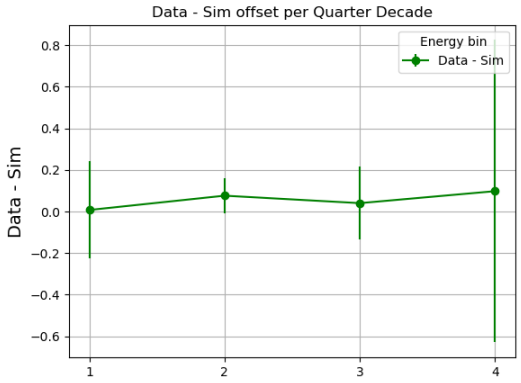

Figure 5.10: Systematic normalized difference between Crab data and simulation.

value is a result of low data counts in the highest energy bins for the Crab.

The comparison for Mrk 421 can be seen in Figure 5.11. Given the nature of Mrk 421 as an extra-galactic source, HAWC only has data in the lower 6 energy bins but it can be seen that the systematic offset found in the Crab example is present in Mrk 421 as well.

5.3.2.2 Simulation Declination Dependence

Lastly, to determine whether there is a systematic offset caused by simulating PS at different declinations, J2031+415 is simulated as a simple power law using the isolated data map. The comparison is shown in Figure 5.12.

For which the systematic difference can be seen in Figure 5.13. Unlike with the data and simulation comparisons, the offset caused by declination is negligible. Therefore,

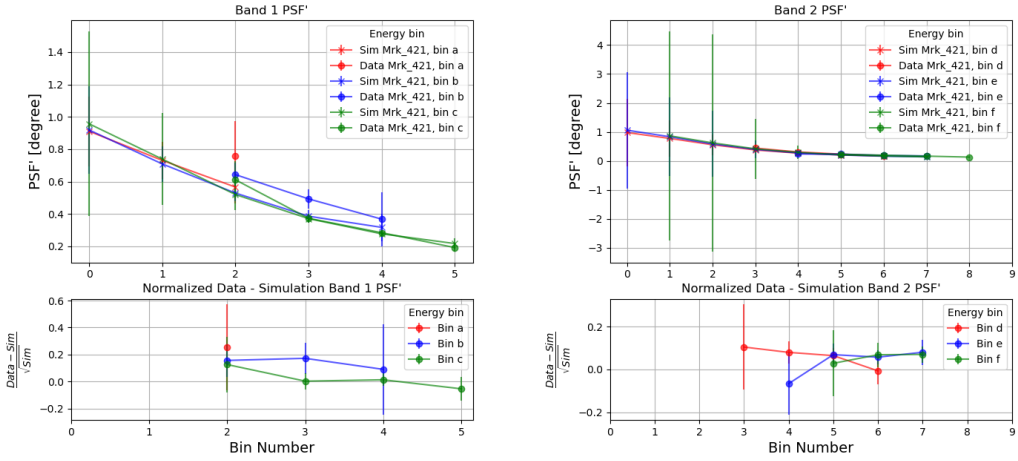

(a) First band.

(b) Second band.

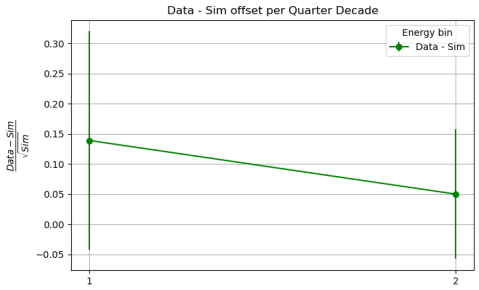

(c) Systematic offset.

Figure 5.11: The PSF' as a function of f_{hit} bins. For Mrk 421, only the first 6 energy bins (a-f) contained significant excess. Figure 5.11(c) shows the systematic offset between data and simulation. It is in rough agreement with the Crab simulation vs data comparison.

the only systematic effect considered is the difference between data and simulated PSF'.

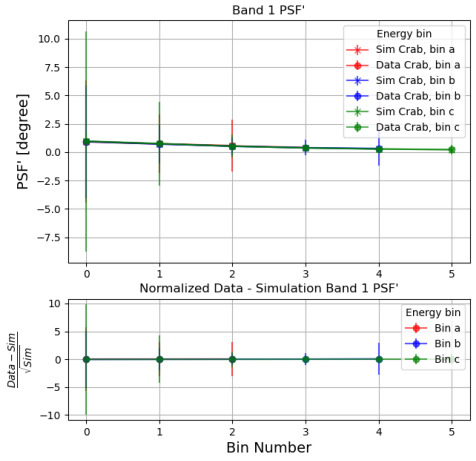

(a) First band.

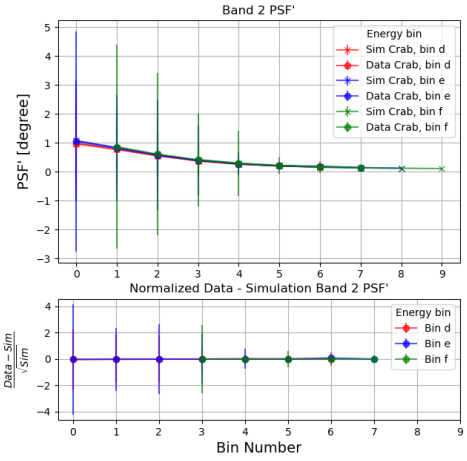

(b) Second band.

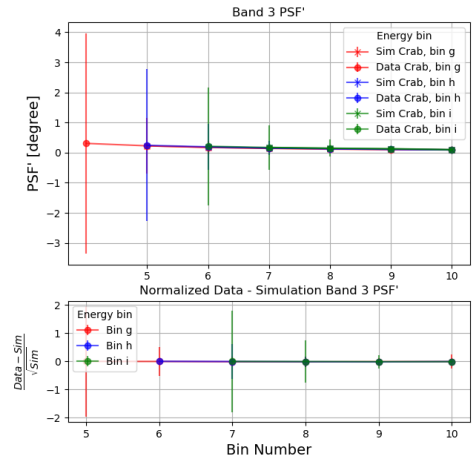

(c) Third band

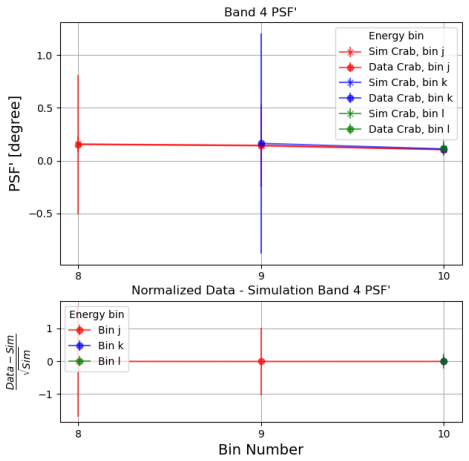

(d) Fourth band.

Figure 5.12: The declination comparison of simulated PSF' between J2031+415 and Crab.

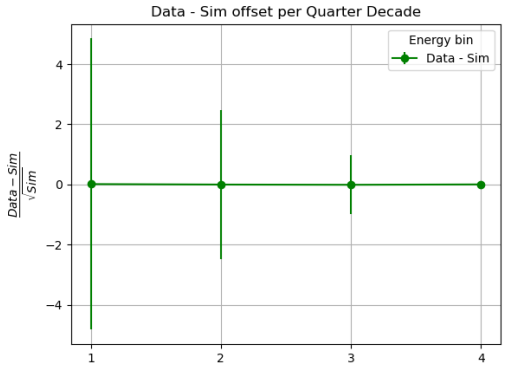

Figure 5.13: Systematic normalized difference between simulated J2031+415 and Crab.

5.3.3 Energy Bands

It is clear from Figure 5.9 that, even for HAWC's brightest source, there is not enough data to perform a bin by bin morphology study. Therefore, energy bands are defined to combine data from a range of energies to allow analysis of dimmer sources. The energy bands are defined in Table 5.7.

Table 5.7
Definition of energy bands with their respective energy ranges

Energy Band	Energy Bins	Energy range (TeV)
1	a, b, c	0.316 - 1.77
2	d, e, f	1.77 - 10
3	g, h, i,	10 - 56.2
4	j, k, l	56.2 - 316

These bands can be divided into two categories: soft and hard bands. Bands 1 and 2 are soft bands where sources with soft (steep) spectra have data while bands 3 and 4

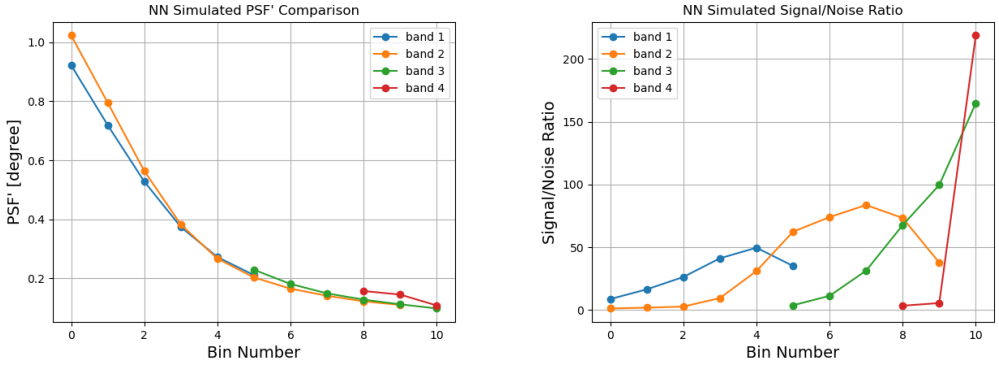

(a) Band PSF'.

(b) Band Signal/Noise Ratio.

Figure 5.14: Simulated PSF' and signal/noise ratio for each energy band. This is done by combining each f_{hit} bin (an example would be bins B1C0Ea, B1C0Eb, and B1C0Ec in band 1) and performing a slice analysis on the new combined bin. This is to determine what bins contribute consistent statistics to the analysis.

are hard bands where only hard (flat) spectra have events.

The next step is to select the bins that minimize the PSF' while still retaining or not significantly reducing the significance of each band. As simulated sources are not limited by events, the simulated Crab is used for bin selection. As it can be seen in Figure 5.14, the PSF' of each f_{hit} bin decreases but the significance (signal/noise ratio) reaches a peak at a certain bin and then decreases. To retain the best possible PSF' and signal/noise ratio, the following criteria are used: the bin with the highest signal/noise ratio is selected and all following (after the highest signal/noise ratio one) are kept. For bins preceding the selected bin, they are selected if their PSF' is roughly within 25% of the selected bin. This criteria is used for bands 1 and 2 where there is an up-down trend but for band 3 the 25% threshold is expanded slightly and for

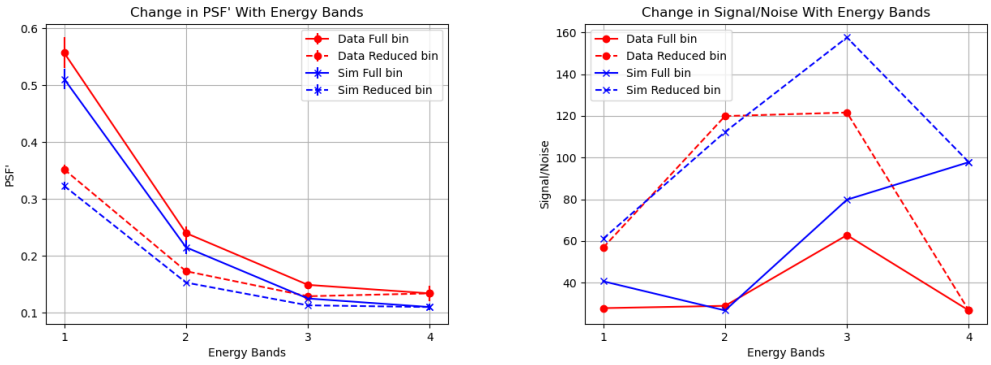

(a) Band PSF'.

(b) Band Signal/Noise Ratio.

Figure 5.15: Simulated PSF' and signal/noise ratio comparison for the full and reduced data along with simulated data. It can be seen that significant improvements are gained in both band PSF' and signal/noise, especially in the lower energy bands.

band 4 all bins are kept to maximize the amount of data. The bin selection for NN is given in Table 5.8 and the band comparison of the simulated Crab is given in Figure 5.15. With these studies completed, an energy morphology study of J2031+415 can be undertaken.

Table 5.8

Final bins selected for NN energy morphology study based off the Crab simulation results. The energy estimator sub-bins are given for reference.

Energy Band	Selected f_{hit} Bins
1 (a, b, c)	3, 4, 5
2 (d, e, f)	6, 7, 8, 9
3 (g, h, i)	8, 9, 10
4 (j, k, l)	8, 9, 10

5.3.4 Results of Energy Morphology Study

As the binning for HAWC is declination dependent, the bins used for Crab and J2031+415 analyzes differ. Therefore, the selected bins used for J2031+415 are based off the reduced bin list for the Crab given in Table 5.8 and include all bins shared between the two sources. The final bins for this analysis are given as follows: Band 1: B3C0Eb B3C0Ec B4C0Ec B5C0Ec, Band 2: B6C0Ed B6C0Ee B6C0Ef B7C0Ee B7C0Ef, Band 3: B8C0Eg B8C0Eh B8C0Ei B9C0Eg B9C0Eh B9C0Ei B10C0Eh B10C0Ei, and Band 4: B8C0Ej B9C0Ej B9C0Ek B10C0Ej B10C0Ek B10C0El. The slicing region is selected by the angle that PSR J2032+4127 and J2031+415's best fit location makes and is determined to be 16.7°. The selected region in the isolated data map is shown in Figure 5.16.

The significance and excess count plots for each band are given in Figures 5.17 and 5.18. One note is that the slicing tool will fit a Gaussian to any data map so a visual inspection of the fit is required to determine the validity of the fit. It can be seen that only Bands 2 and 3 return a valid fit from the slicing form of the energy morphology analysis. This corresponds to emission from the 1.77-56.2 TeV range, which is confirmed by the energy range study performed in Section 5.2.1.

Now that the raw Gaussian width for each band (if a valid fit result was given) has

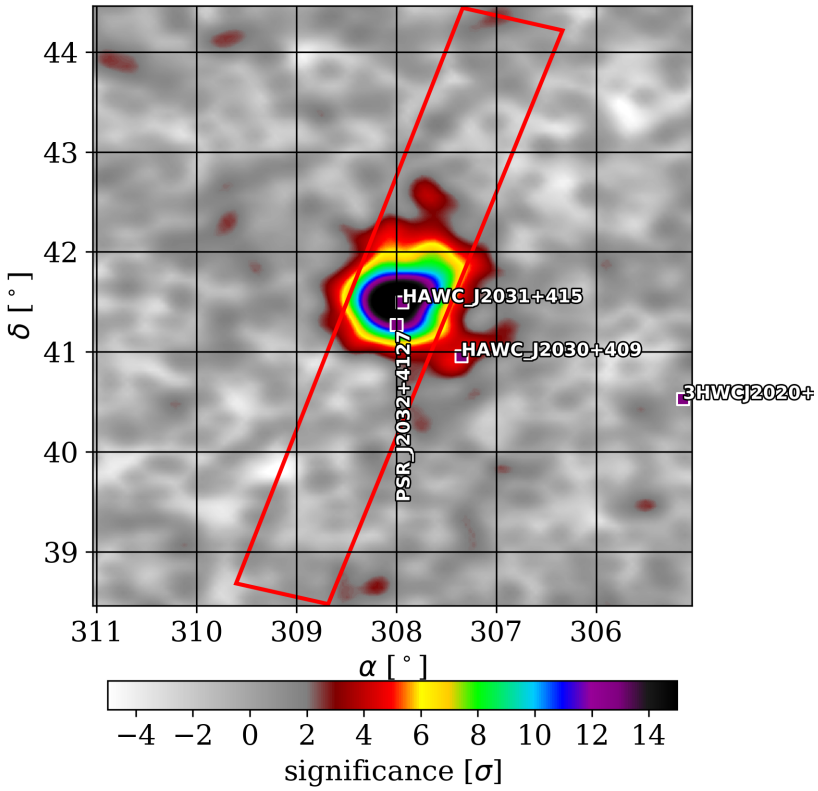

Figure 5.16: The data map and slicing region used for this analysis. The Cocoon (J2030+409) and Gamma Cygni (J2020+403) labels are kept for reference to the full 3 source model

been determined, the final step of the morphology study can be taken. It was seen from the systematic studies that even a point source like the Crab has some intrinsic width like with the PSF definition and leads to a smearing effect that applies to any analysis using this slicing method. Therefore, to determine the true PSF' width of the emission region, the observed width of the source is subtracted in quadrature by the systematic effect caused by the smearing and what the difference between data

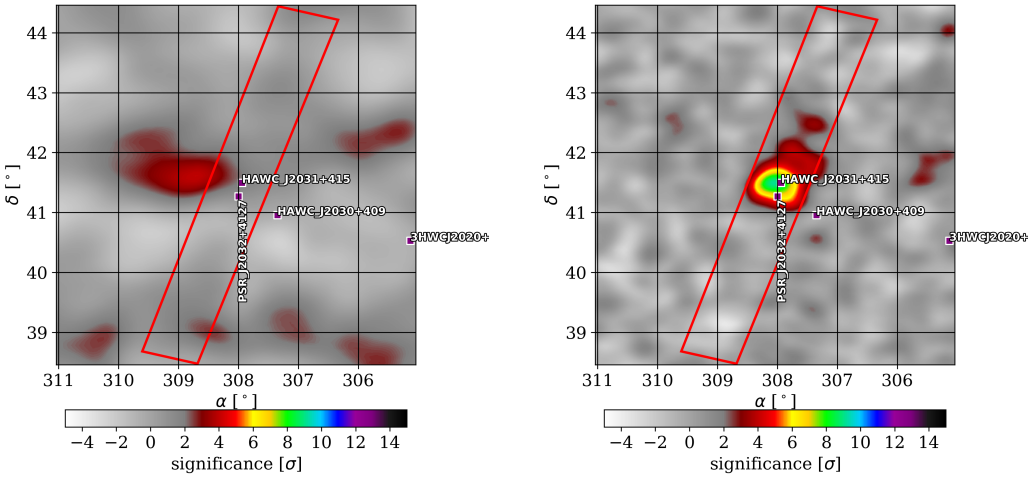

(a) First band significance map.

(b) Second band significance map.

(c) Third band significance map.

(d) Fourth band significance map.

Figure 5.17: Significance maps of the region in each reduced energy band. Bands 1 and 4 have insufficient data while there is a significant excess in Bands 2 and 3. This is reflected in the energy range study from Section 5.2.1. Additionally, Band 4's different background is due to the extremely low probability of a background event at energies > 56 TeV.

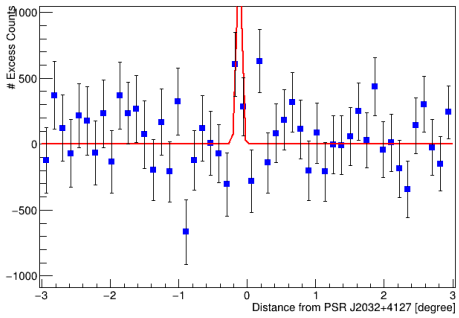

(a) First band excess count map.

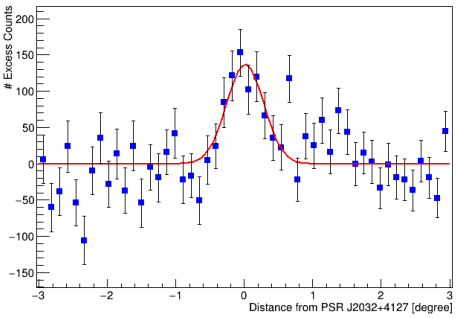

(b) Second band excess count map.

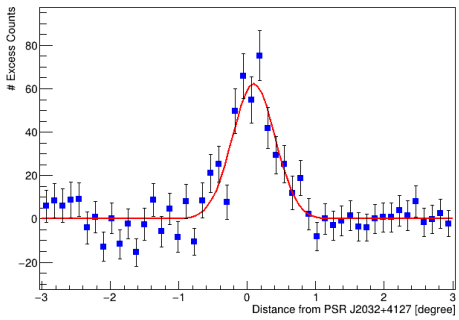

(c) Third band excess count map.

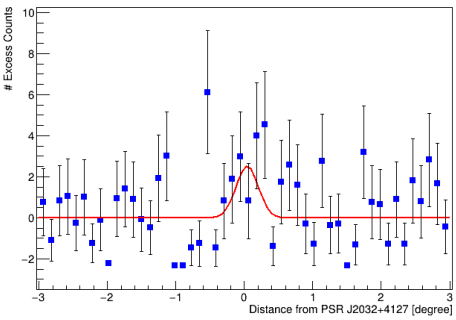

(d) Fourth band excess count map.

Figure 5.18: The excess count profiles corresponding to the significance maps shown above. As visually noted, Bands 1 and 4 are confirmed to have insufficient data to determine a emission region width.

and simulation was determined to be. This is given as

$$\sigma_{\text{true}} = \sqrt{(\sigma_{\text{fit}})^2 - (\sigma_{\text{PS}} + \sigma_{\text{offset}})^2} \tag{5.2}$$

where σ_{fit} is the raw PSF' fit found in the excess count profile (if valid), σ_{sim} is the simulated PS for that band's PSF', and σ_{offset} is the systematic difference shown and is unique to each band. It was found that for σ_{offset} the only contributing offset was

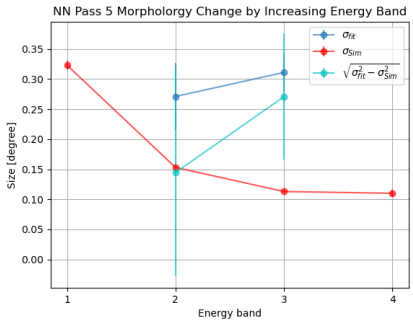

(a) NN emission width.

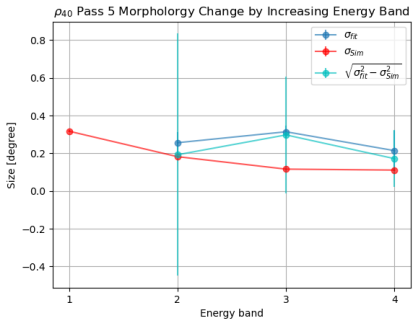

(b) ρ_{40} emission width.

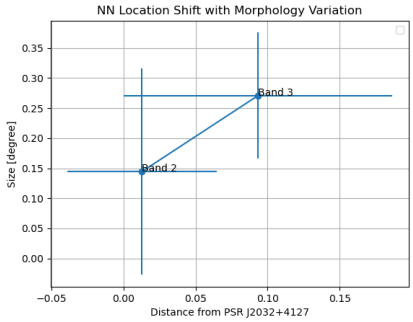

(c) NN location shift.

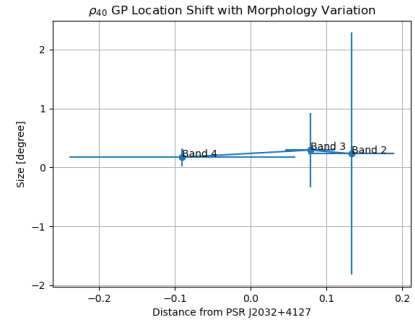

(d) ρ_{40} location shift.

Figure 5.19: The final morphological results for J2031+415. It should be noted that while the ρ_{40} estimator has a fit for band 4, it is a very noisy result (see Figure C.10) and is on the threshold of ρ_{40}'s energy range of 55 TeV.

the data - simulation study done on the Crab and so is the sole contributor to σ_{offset}. Error propagation for this process follows the rules outlined in [64]. The final width and distance from PSR J2032+4127 for both NN and ρ_{40} are given in Figure 5.19. The differences between the two estimators will contribute to the systematic uncertainties when those are properly determined. From Figure 5.19 it can be seen that there is no decisive energy morphology of J2031+415. Likewise, there is no clear tread with the positional shift of the emission.

Chapter 6

Conclusions and Future Work

In this thesis an analysis of HAWC J2031+415 in the 1-100 TeV energy range was presented. The three sources considered: HAWC J2031+415 (PWN), HAWC J2030+409 (Cocoon), and HAWC J2020+403 (Gamma Cygni), were modelled using both systematic source search and spectral modelling studies. HAWC J2031+415's best fit spectral fit was found to be a power law with an exponential cut-off with a cut-off of 24^{24}_{-13}TeV, confirming VERITAS' prediction of a cut-off in the 10's of TeV and hinting at a PWN.

Once the region was modelled, HAWC J2031+415 was isolated by subtracting out the emission from the other sources and an energy morphology study was performed. This study counted the excess events measured by HAWC in 4 distinct energy bands:

0.316 - 1.78 TeV, 1.78 - 10 TeV, 10 - 56.2 TeV, and 56.2 - 316 TeV. The results of the study are inconclusive where only bands 2 and 3 had valid fits for the NN and bands 2, 3, and 4 (weak fit) for ρ_{40}. Additionally the positional shift of the emission region center was inconclusive. Therefore there is not confirmation of HAWC J2031+415 being a PWN and more data is needed to confirm the PWN hypothesis.

References

[1] MicroWorlds. Electromagnetic spectrum. https://www2.lbl.gov/MicroWorlds/ALSTool/EMSpec/EMSpec2.html.

[2] Stephan Rosswog and Marcus Brüggen. *Introduction to High-Energy Astrophysics*. Cambridge University Press, 2007.

[3] Ilya Obodovskiy. *Radiation*. Elsevier, 2019.

[4] Bernlöhr Konrad. Shower detection. https://www.mpi-hd.mpg.de/hfm/CosmicRay/ShowerDetection.html.

[5] NSF. Veritas discovers very high energy gamma rays from the starburst galaxy m82. https://www.nsf.gov/news/news_summ.jsp?org=NSF&cntn_id=115836&preview=false.

[6] A. Heger, C. L. Fryer, S. E. Woosley, N. Langer, and D. H. Hartmann. How Massive Single Stars End Their Life. *ApJ*, 591(1):288–300, July 2003.

[7] E. Aliu et al. Observation of pulsed gamma-rays above 25 gev from the crab pulsar with magic. *Science*, 322:1221–1224, 2008.

[8] Takahiro Sudoh, Tim Linden, and John F. Beacom. Tev halos are everywhere: Prospects for new discoveries. *Phys. Rev. D*, 100:043016, Aug 2019.

[9] F. A. Aharonian. *Very High Energy Cosmic Gamma Radiation: A Crucial Window on the Extreme Universe*. Peking University Press, 2012.

[10] F. Aharonian et al. The unidentified tev source (tev j2032+4130) and surrounding field: Final hegra iact-system results. *A&A*, 431(1):197–202, 2005.

[11] A Albert and et al. Spectrum and morphology of the very-high-energy source hawc j2019+368. *The Astrophysical Journal*, 911:143, 04 2021.

[12] E. Aliu et al. OBSERVATIONS OF THE UNIDENTIFIED GAMMA-RAY SOURCE TeV j2032+4130 BY VERITAS. *The Astrophysical Journal*, 783(1):16, feb 2014.

[13] Cong Li. Detection of emission from Cygnus Cocoon above 100TeV with LHAASO. *PoS*, ICRC2021:843, 2021.

[14] Ian Herzog. Spectral and energy morphology analysis study of hawc j2031+415. *Proceedings of 37th International Cosmic Ray Conference — PoS(ICRC2021)*, 2021.

[15] Binita Hona. *Cosmic-Ray Acceleration in the Cygnus OB2 Stellar Association*. PhD thesis, Michigan Technological University, United States, January 2020.

[16] Adian E. Raftery and Robert E. Kass. Bayes factors. *Journal of the American Statistical Association*, 90(430):773–795, 1995.

[17] Merriam-Webster. Astrophysics. `https://www.merriam-webster.com/dictionary/astrophysics`.

[18] Thomas K. Gaisser, Ralph Engel, and Elisa Resconi. *Cosmic Rays and Particle Physics 2nd Edition*. Cambridge University Press, 2016.

[19] M. Bustamante et al. High-energy cosmic-ray acceleration. *2009 CERN-Latin American School of High-Energy Physics*, pages 533–540, 2009.

[20] Malcolm S. Longair. *High Energy Astrophysics*. Cambridge University Press, 3 edition, 2011.

[21] A. R. Bell. The acceleration of cosmic rays in shock fronts - I. *Monthly Notices of the Royal Astronomical Society*, 182:147–156, January 1978.

[22] Vikas Joshi. *Reconstruction and analysis of highest energy γ-rays and its application to pulsar wind nebulae*. PhD thesis, Heidelberg University, Germany, January 2019.

[23] O. Klein and T. Nishina. Über die Streuung von Strahlung durch freie Elektronen nach der neuen relativistischen Quantendynamik von Dirac. *Zeitschrift fur Physik*, 52(11-12):853–868, November 1929.

[24] R. Miskimen. Supernova Remnants at High Energy. *Annual Review of Astronomy and Astrophysics*, 46:89–126, 2008.

[25] G. E. Romero. Gamma Rays from Star-Forming Regions. In *AIP Conference Proceedings*, volume 1085, 2008.

[26] A. M. Bykov and G. D. Fleishman. On non-thermal particle generation in superbubbles. *Monthly Notices of the Royal Astronomical Society*, 255(2):269–275, 03 1992.

[27] Z. Cao, J.A. Aharonian, et al. Ultrahigh-energy photons up to 1.4 petaelectronvolts from 12 γ-ray Galactic sources. *Nature*, 594:33–36, June 2021.

[28] F Aharonian, J Buckley, T Kifune, and G Sinnis. High energy astrophysics with ground-based gamma ray detectors. *Reports on Progress in Physics*, 71(9):096901, Aug 2008.

[29] Yury Verzilov, Kentaro Ochiai, Chuzo Kutsukake, and Takeo Nishitani. Cherenkov detector of the water flow activated by 14 mev neutrons. 2004.

[30] S.M.Bradbury. The very energetic radiation imaging telescope array. In *Proceedings of the 26th ICRC*, 1999.

[31] Juan Cortina. Status and First Results of the Magic Telescope. *Astrophysics and Space Science*, 297(1-4):245–255, June 2005.

[32] Magic - major atmospheric gamma imaging cherenkov telescope. `https://www.mpp.mpg.de/forschung/astroteilchenphysik-und-kosmologie/magic-und-cta-gammastrahlenteleskope/magic`.

[33] M. Amenomori et al. Perfrmance of the tibet-iii air shower array. In *Proceedings of the 28th International Cosmic Ray Conference*, 2003.

[34] Utz Kramar. *Encyclopedia of Spectroscopy and Spectrometry.* Elsevier, 1999.

[35] C Bacci, KZ Bao, F Barone, B Bartoli, P Bernardini, R Buonomo, S Bussino, E Calloni, BY Cao, R Cardarelli, et al. High altitude test of rpcs for the argo ybj experiment. *Nuclear instruments and methods in physics research section a: accelerators, spectrometers, detectors and associated equipment*, 443(2-3):342–350, 2000.

[36] CERN. Resistive plate chambers. `https://cms.cern/detector/detecting-muons/resistive-plate-chambers`.

[37] G. Sinnis. MILAGRO: a Low Energy Threshold Extensive Air Shower Array. In Patrick Fleury and Giuseppe Vacanti, editors, *Towards a Major Atmospheric Cerenkov Detector for TeV Astro/particle Physics*, page 305, June 1992.

[38] A. Abeysekara, A. Albert, Romulo Alfaro, C. Alvarez, J. Álvarez, J. Camacho, Roberto Arceo, J. Arteaga-Velázquez, Arun Babu K. P., D. Rojas, Hugo Ayala Solares, Vardan Baghmanyan, E. Belmont-Moreno, S. BenZvi, Chad Brisbois, Karen Salome Caballero Mora, T. Capistrán, A. Carramiñana, Sabrina Casanova, and H. Zhou. Measurement of the crab nebula spectrum past 100 tev with hawc. *The Astrophysical Journal*, 881:134, 08 2019.

[39] Bradley W. Carroll and Dale A. Ostlie. *An Introduction to Modern Astrophysics*. Pearson Education Inc., 2007.

[40] J. W. T. Hessls et al. A radio pulsar spinning at 716 hz. *Science*, 311:1901–1904, 2006.

[41] Bryan M. Gaensler and Patrick O. Slane. The evolution and structure of pulsar wind nebulae. *Annual Review of Astronomy and Astrophysics*, 44:14–47, 2006.

[42] Peter Goldreich and William H. Julian. Pulsar electrodynamics. *The Astrophysical Journal*, 157:869–880, 1969.

[43] John G. Kirk, Yuri Lyubarsky, and Jerome Petri. The Theory of Pulsar Winds and Nebulae. In Werner Becker, editor, *Astrophysics and Space Science Library*, volume 357 of *Astrophysics and Space Science Library*, page 421, January 2009.

[44] M. A. Ruderman and P. G. Sutherland. Theory of pulsars: polar gaps, sparks, and coherent microwave radiation. *ApJ*, 196:51–72, February 1975.

[45] P. A. Sturrock. A Model of Pulsars. *ApJ*, 164:529, March 1971.

[46] Bryan M. Gaensler and Patrick O. Slane. The Evolution and Structure of Pulsar Wind Nebulae. *Annual Review of Astronomy & Astrophysics*, 44(1):17–47, September 2006.

[47] S. P. Reynolds and R. A. Chevalier. Evolution of pulsar-driven supernova remnants. *ApJ*, 278:630–648, March 1984.

[48] E. Swaluw, Turlough Downes, and Ronan Keegan. An evolutionary model for pulsar-driven supernova remnants. a hydrodynamical model. *Astronomy & Astrophysics - ASTRON ASTROPHYS*, 420:937–944, 06 2004.

[49] H. E. S. S. Collaboration, H. Abdalla, et al. Deeper H.E.S.S. observations of Vela Junior (RX J0852.0-4622): Morphology studies and resolved spectroscopy. *Astronomy & Astrophysics*, 612:A7, April 2018.

[50] T. C. Weekes, M. F. Cawley, D. J. Fegan, K. G. Gibbs, A. M. Hillas, P. W. Kowk, R. C. Lamb, D. A. Lewis, D. Macomb, N. A. Porter, P. T. Reynolds, and G. Vacanti. Observation of TeV Gamma Rays from the Crab Nebula Using the Atmospheric Cerenkov Imaging Technique. *ApJ*, 342:379, July 1989.

[51] A. A. Abdo et al. Fermi/Large Area Telescope Bright Gamma-Ray Source List. *ApJs*, 183(1):46–66, July 2009.

[52] Andrew Lyne, Ben Stappers, Michael Keith, Paul Ray, Mônica Kerr, Fernando Camilo, and Tyrel Johnson. The binary nature of PSR J2032+4127. *Monthly Notices of the Royal Astronomical Society*, 451, 2015.

[53] N. Tetzlaff, R. Neuhäuser, and M. M. Hohle. A catalogue of young runaway Hipparcos stars within 3 kpc from the Sun. *Monthly Notices of the Royal Astronomical Society*, 410(1):190–200, 12 2010.

[54] A. U. Abeysekara et al. Periastron Observations of TeV Gamma-Ray Emission from a Binary System with a 50-year Period. *ApJl*, 867(1):L19, November 2018.

[55] Giacomo Vianello, Robert J. Lauer, et al. The Multi-Mission Maximum Likelihood framework (3ML). In *Proceedings of Science*, 2015.

[56] Željko Ivezicć, Jacob T. VanderPlas Andrew J. Connolly, and Alexander Gray. *Statistics, Data Mining, and Machine Learning in Astronomy.* Princeton University Press, 2014.

[57] G. Vianello, J. M. Burgess, N. Di Lalla, N. Omodei, and H. Fleischhack. Builtin functions astromodels. `https://astromodels.readthedocs.io/en/latest/function_docs/functions.html`.

[58] A Abramowski and H. E. S. S. Collaboration. Diffuse Galactic gamma-ray emission with H.E.S.S. *Physical Review*, 90(12):122007, December 2014.

[59] S. S. Wilks. The large-sample distribution of the likelihood ratio for testing composite hypotheses. *The Annals of Mathematical Statistics*, 9, 1938.

[60] P Speckmayer, A Höcker, J Stelzer, and H Voss. The toolkit for multivariate data analysis, TMVA 4. *Journal of Physics: Conference Series*, 219(3):032057, apr 2010.

[61] M. Ackermann et al. *The Astrophysical Journal*, 843, 2017.

[62] A.U. Abeysekara et al. HAWC observations of the acceleration of very-high-energy cosmic rays in the Cygnus Cocoon. *Nature Astronomy*, 5:465–471, March 2021.

[63] A. U. Abeysekara et al. Extended gamma-ray sources around pulsars constrain the origin of the positron flux at Earth. *Science*, 358(6365):911–914, November 2017.

[64] John Taylor. *Introduction to Error Analysis, the Study of Uncertainties in Physical Measurements, 2nd Edition*. 1997.

[65] Camden Ertley. *Studying the polarization of hard x-ray solar flares with the Gamma RAy Polarimeter Experiment (GRAPE)*. PhD thesis, University of New Hampshire, January 2014.

[66] The HAWC Collaboration. Cosmic rays. `https://www.hawc-observatory.org/science/cosmicrays.php`.

[67] S. P. Swordy. The Energy Spectra and Anisotropies of Cosmic Rays. *Space Science Reviews*, 99:85–94, 2001.

[68] R. Miskimen. Neutral Pion Decay. *Annual Review of Nuclear and Particle Science*, 61:1–21, 2011.

[69] Camden Ertley. Supernova Remnants at High Energy. 46:89–126, 2008.

Appendix A

Systematic Source Search using the f_{hit} Estimator

This section shows the process used in determining the final model of the region. The plots shown are the model, residual, and 1D histogram of each step taken. Additionally, the new source location and significance are also given. The study concludes when the $\Delta TS < 16$ threshold is reached. One note is that while DBE + 3 EXT + 2 PS was tested, the fit only partially converged and gave a $\Delta TS = 2$. This was most likely due to the dim nature of the new PS location at $\sigma = 3.44$.

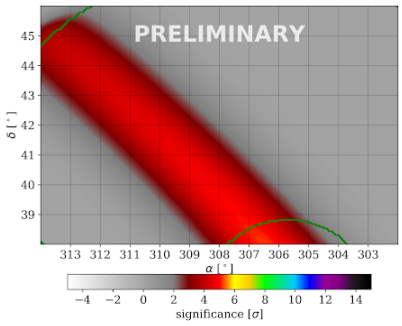

(a) Model significance map.

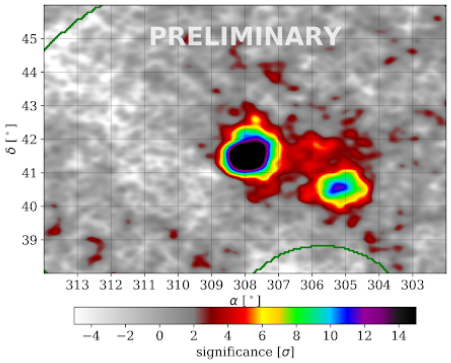

(b) Residual significance map.

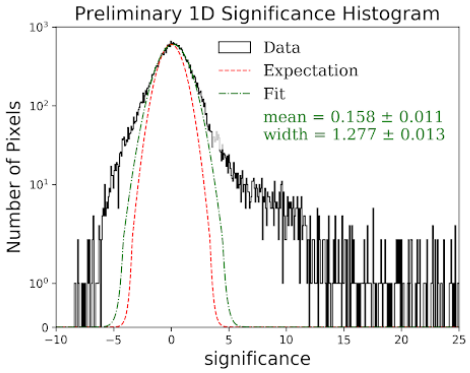

(c) The residual 1D histogram.

Figure A.1: DBE only model. New source is at 307.92, 41.51 and significance is 29.00. $\Delta TS = 0$ (initial model

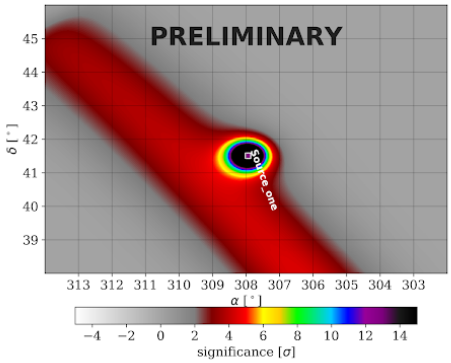

(a) Model significance map.

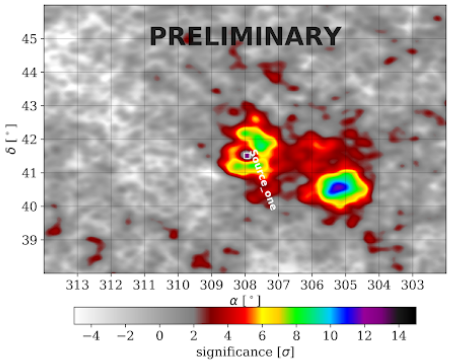

(b) Residual significance map.

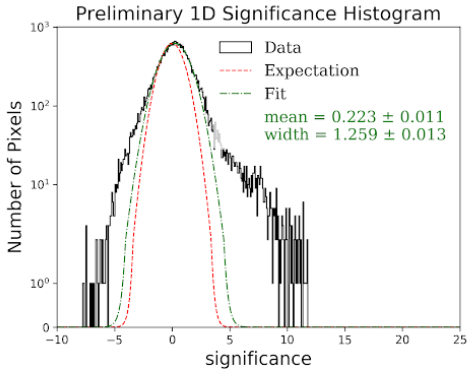

(c) The residual 1D histogram.

Figure A.2: DBE + 1 PS model. New source is at 305.16, 40.57 and significance is 11.72. $\Delta TS = 930$

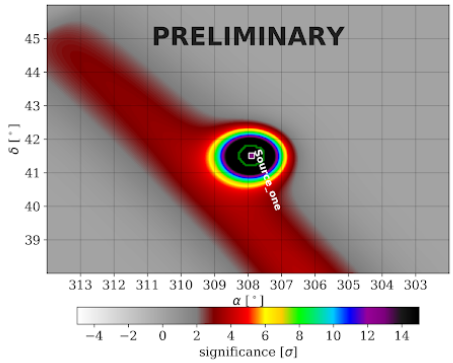

(a) Model significance map.

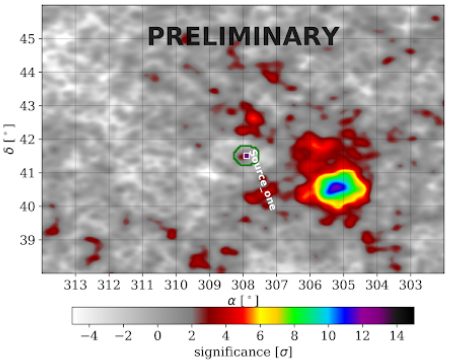

(b) Residual significance map.

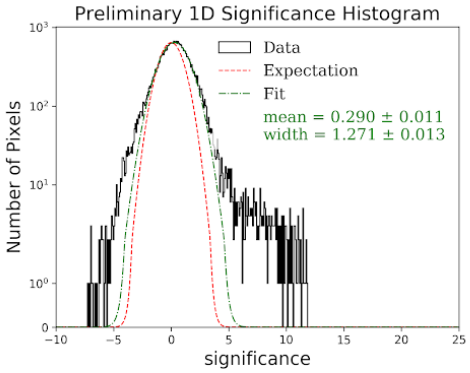

(c) The residual 1D histogram.

Figure A.3: DBE + 1 EXT model. New source is at 305.16, 40.57 and significance is 11.78. $\Delta TS = 357$

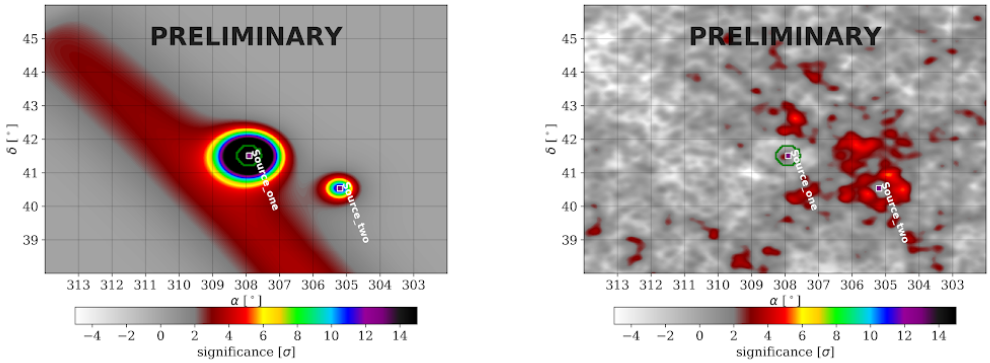

(a) Model significance map.

(b) Residual significance map.

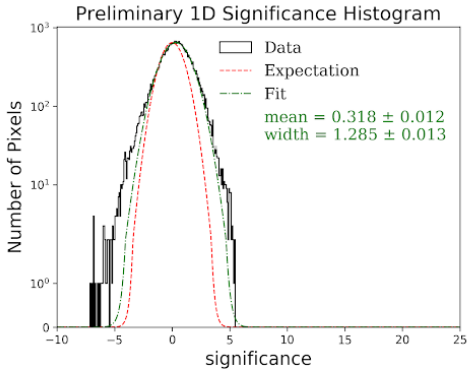

(c) The residual 1D histogram.

Figure A.4: DBE + 1 EXT + 1 PS model. New source is at 304.94, 40.92 and significance is 5.72. $\Delta TS = 199$

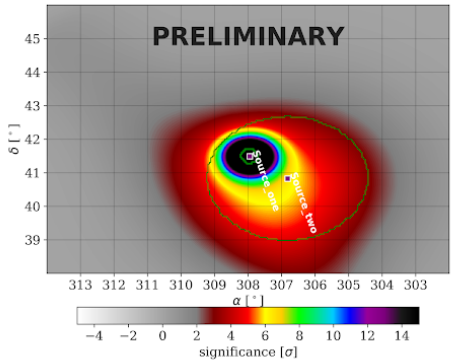

(a) Model significance map.

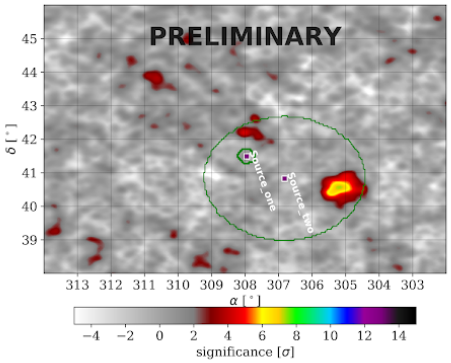

(b) Residual significance map.

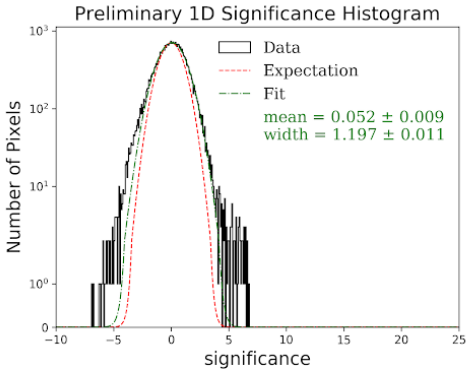

(c) The residual 1D histogram.

Figure A.5: DBE + 2 EXT model. New source is at 305.16, 40.57 and significance is 6.74. $\Delta TS = 197$

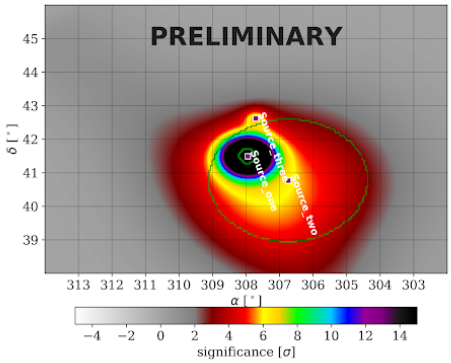

(a) Model significance map.

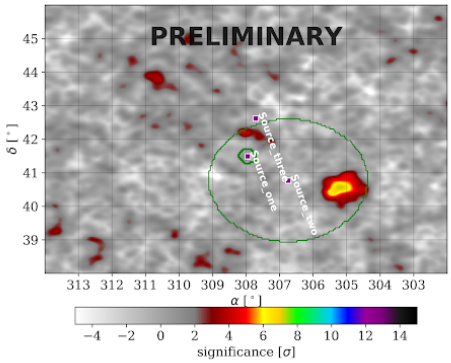

(b) Residual significance map.

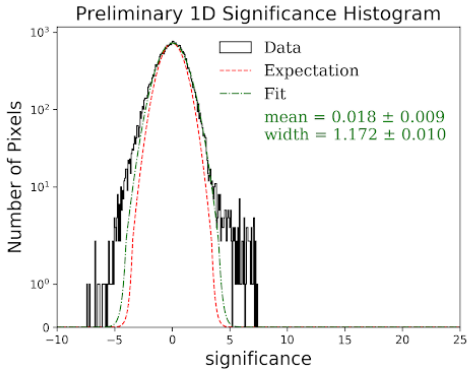

(c) The residual 1D histogram.

Figure A.6: DBE + 2 EXT + 1 PS model. New source is at 305.16, 40.57 and is 7.38. $\Delta TS = 26$

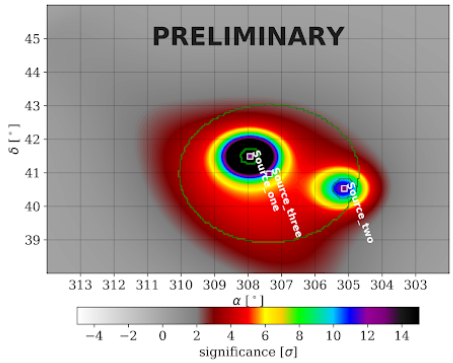

(a) Model significance map.

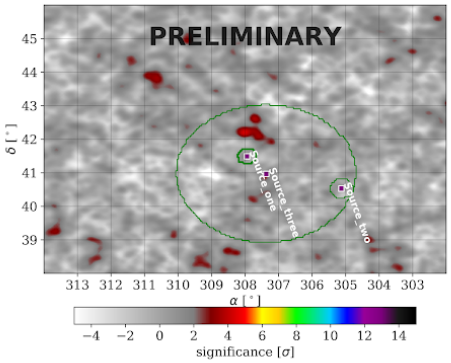

(b) Residual significance map.

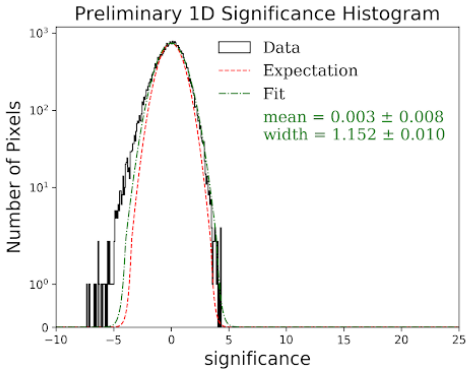

(c) The residual 1D histogram.

Figure A.7: DBE + 3 EXT model. New source is at 308.05, 42.21 and is 4.35. $\Delta TS = 107$

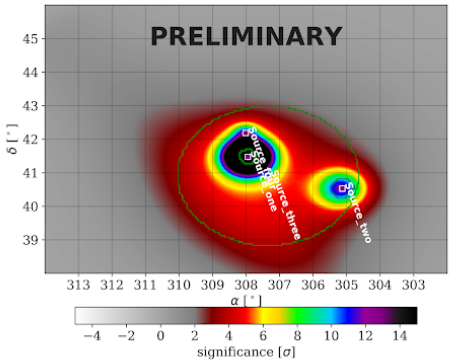

(a) Model significance map.

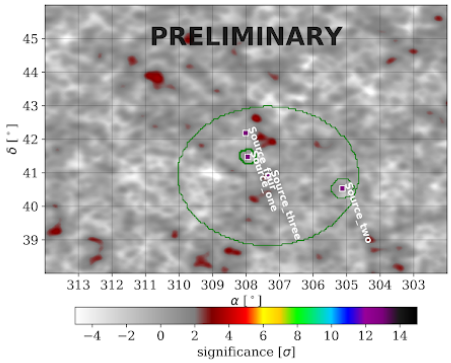

(b) Residual significance map.

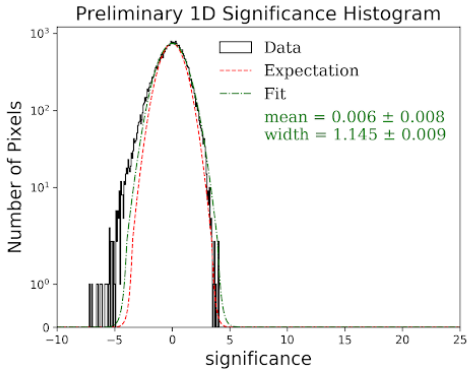

(c) The residual 1D histogram.

Figure A.8: DBE + 3 EXT + 1 PS model. New source is at 307.72, 42.61 and is 3.48. $\Delta TS = 23$

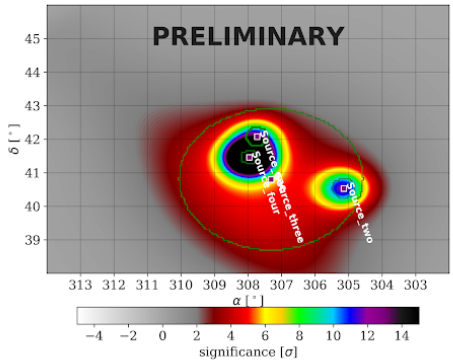

(a) Model significance map.

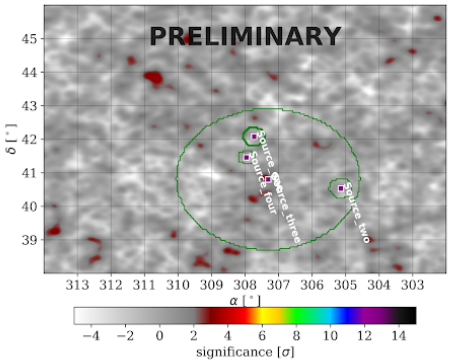

(b) Residual significance map.

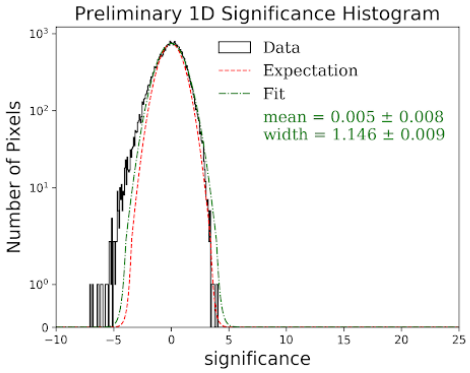

(c) The residual 1D histogram.

Figure A.9: DBE + 4 EXT model. New source is at 310.61, 43.85 and is 3.44. $\Delta TS = 4$. Rejected

Appendix B

NN plots

This brief section shows the initial significance map present in the NN estimator as well as the results of the NN energy range study. Additionally, the bins used are B2C0Ea B2C0Eb B2C0Ec B2C0Ed B2C0Ee B3C0Eb B3C0Ec B3C0Ed B3C0Ee B3C0Ef B4C0Ec B4C0Ed B4C0Ee B4C0Ef B4C0Eg B5C0Ec B5C0Ed B5C0Ee B5C0Ef B5C0Eg B5C0Eh B6C0Ed B6C0Ee B6C0Ef B6C0Eg B6C0Eh B6C0Ei B7C0Ee B7C0Ef B7C0Eg B7C0Eh B7C0Ei B8C0Eg B8C0Eh B8C0Ei B8C0Ej B9C0Eg B9C0Eh B9C0Ei B9C0Ej B9C0Ek B10C0Eh B10C0Ei B10C0Ej B10C0Ek B10C0El.

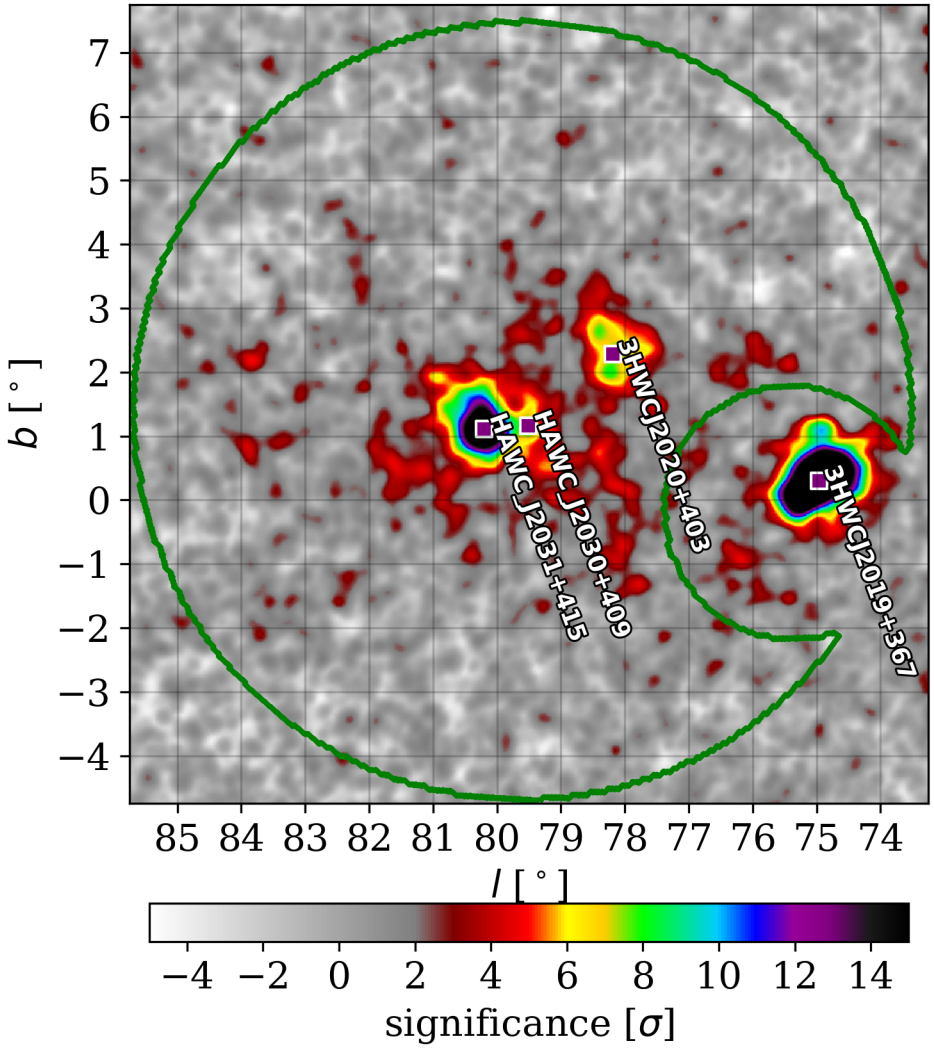

Figure B.1: The data set available in the NN map.

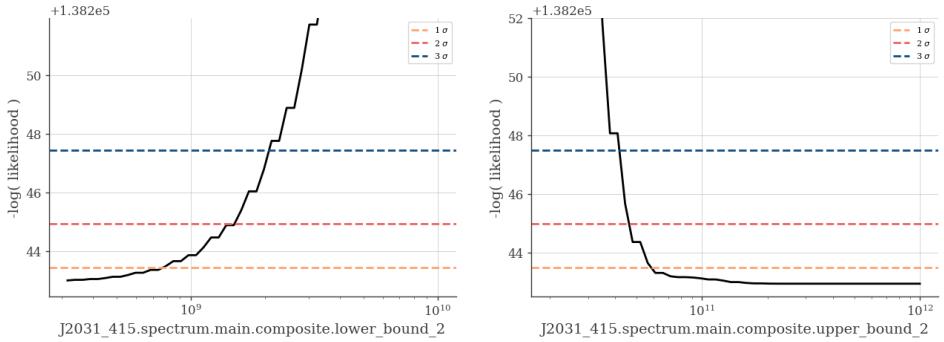

(a) J2031+415 lower bound.

(b) J2031+415 upper bound

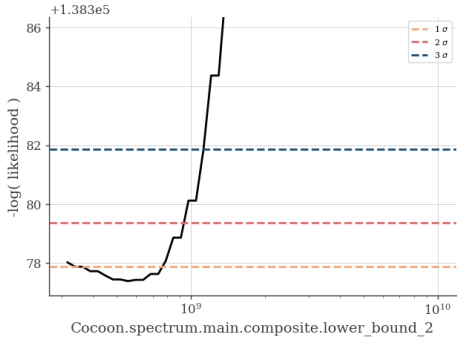

(c) Cocoon lower bound

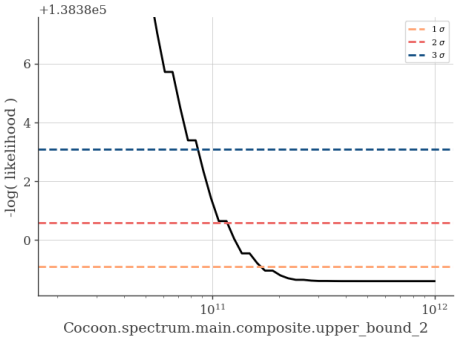

(d) Cocoon upper bound

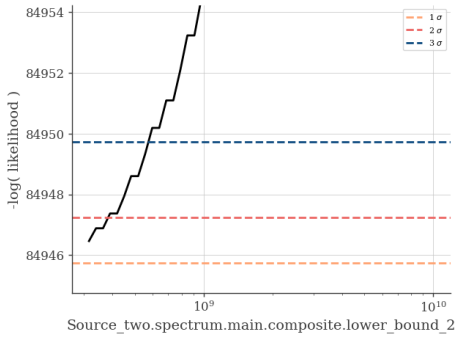

(e) Gamma Cygni lower bound

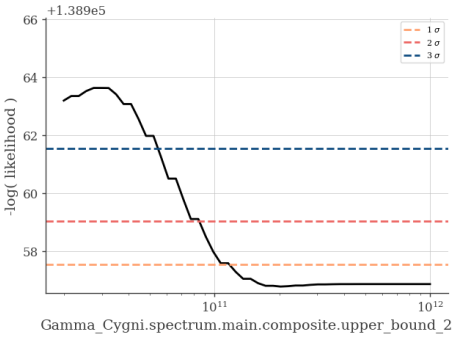

(f) Gamma Cygni upper bound

Figure B.2: The energy range study of the three sources using the NN data set

Appendix C

Systematic PSF' studies with ρ_{40} Estimator

The morphology study steps as done with the ρ_{40} map. Also included is the initial significance of the region. The morphology study steps are the same ones discussed in Chapter 5. Additionally, the bins used for ρ_{40} are B2C0Eb B2C0Ec B2C0Ed B3C0Eb B3C0Ec B3C0Ed B3C0Ee B3C0Ef B3C0Eg B4C0Ec B4C0Ed B4C0Ee B4C0Ef B4C0Eg B5C0Ec B5C0Ed B5C0Ee B5C0Ef B5C0Eg B5C0Eh B6C0Ed B6C0Ee B6C0Ef B6C0Eg B6C0Eh B7C0Ef B7C0Eg B7C0Eh B7C0Ei B8C0Ef B8C0Eg B8C0Eh B8C0Ei B8C0Ej B9C0Eg B9C0Eh B9C0Ei B9C0Ej B9C0Ek B10C0Eg B10C0Eh B10C0Ei B10C0Ej B10C0Ek B10C0El

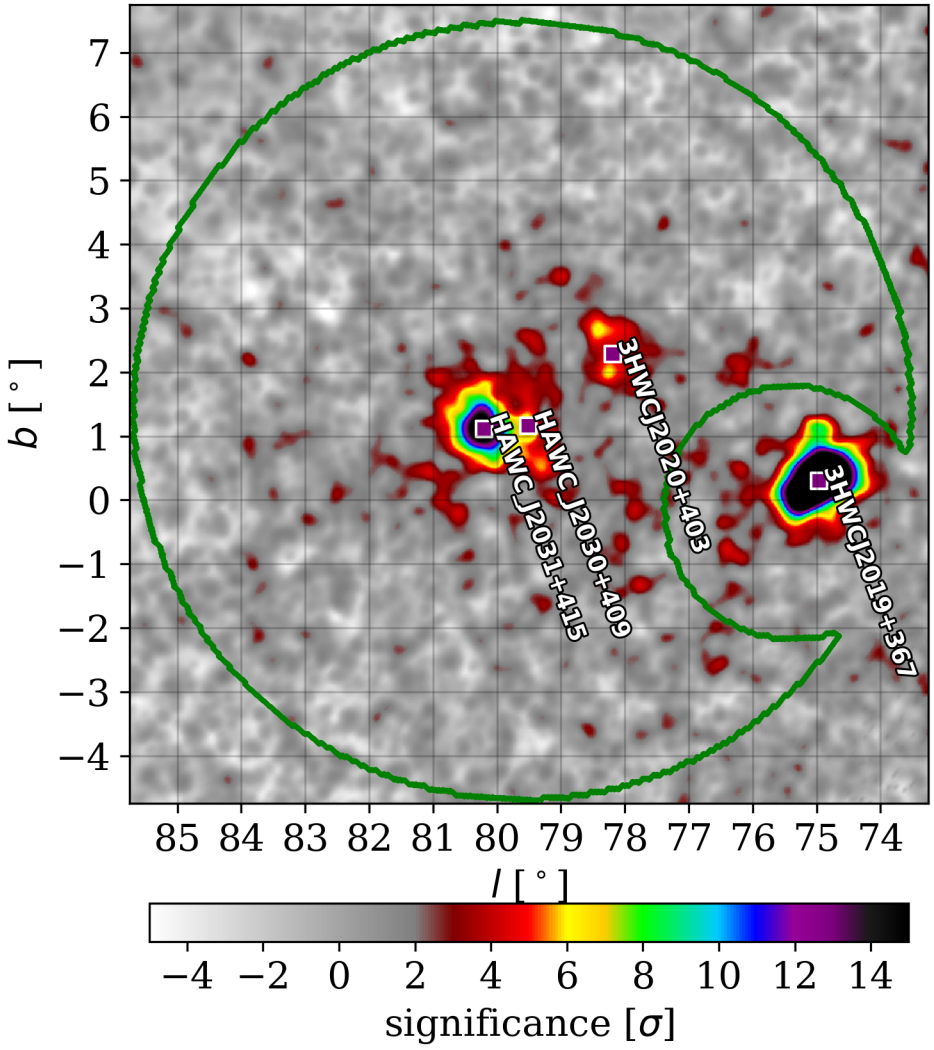

Figure C.1: The data set available in the ρ_{40} map.

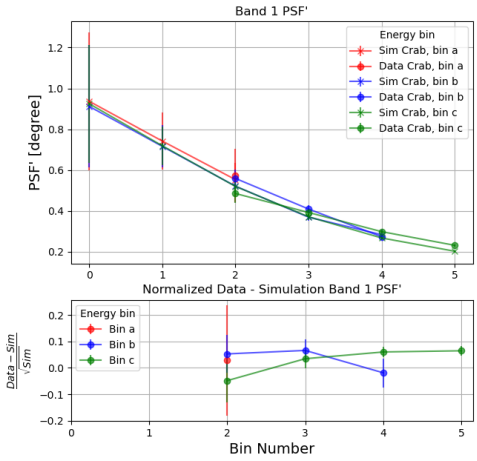

(a) First band.

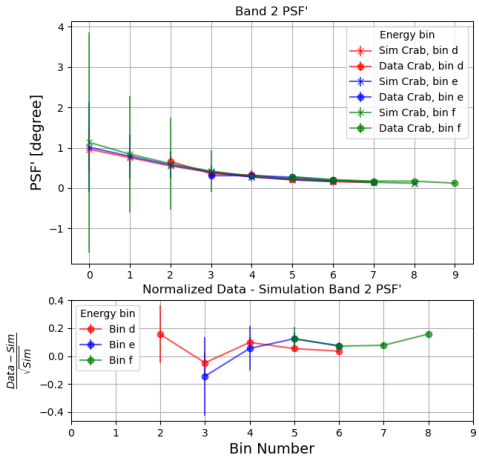

(b) Second band.

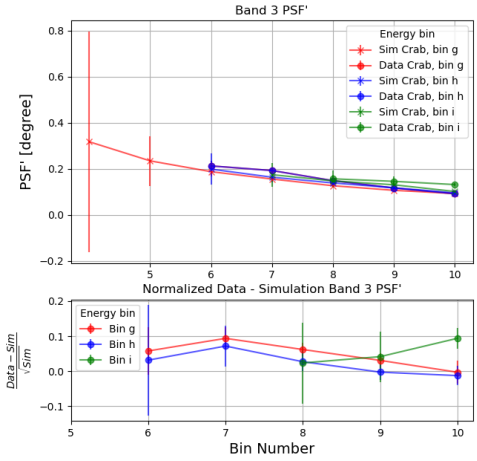

(c) Third band

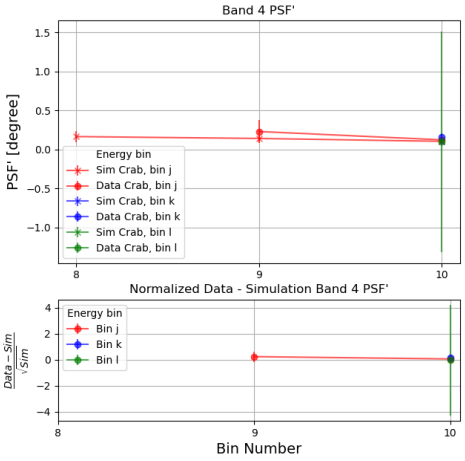

(d) Fourth band.

Figure C.2: The PSF' as a function of f_{hit} bins. Each plot has three of the decade bins a-l and in the top plot the comparison between data and simulated PSF' is shown. Note that not all data bins have a PSF'. The lower plot is the normalized difference between data and simulation to determine if there is a systematic difference between data and simulation.

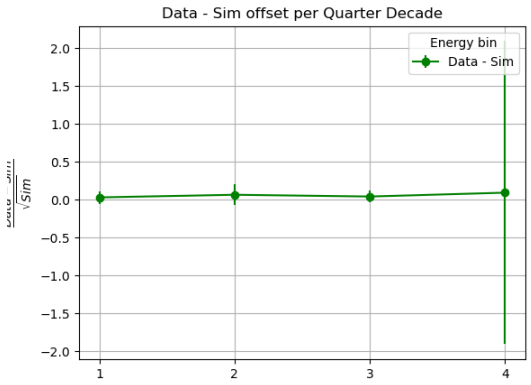

Figure C.3: Systematic normalized difference between Crab data and simulation.

Table C.1

Final bins selected for ρ_{40} energy morphology study based off the Crab simulation results. The energy estimator sub-bins is given for reference.

Energy Band	Selected f_{hit} Bins
1 (a, b, c)	3, 4, 5
2 (d, e, f)	5, 6, 7, 8
3 (g, h, i)	8, 9, 10
4 (j, k, l)	8, 9, 10

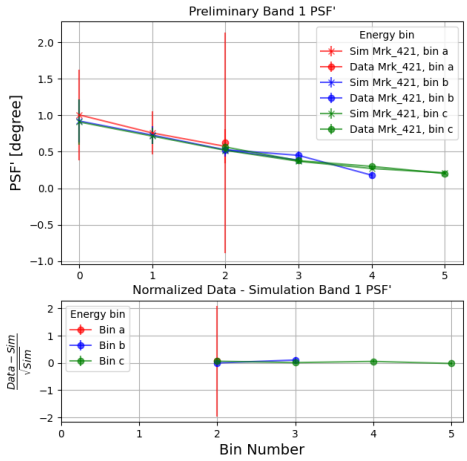

(a) First band.

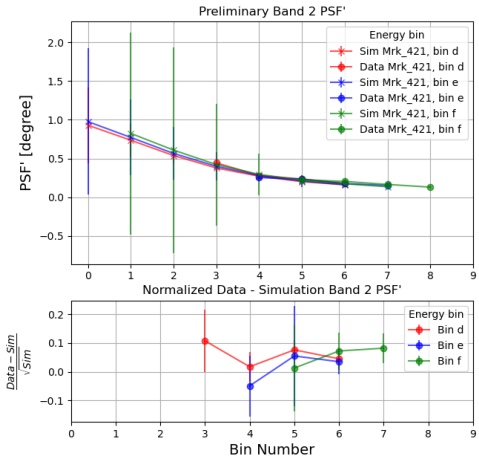

(b) Second band.

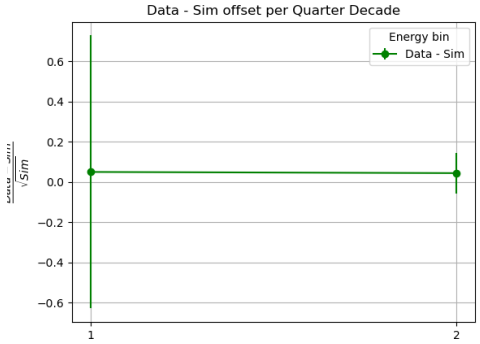

(c) Systematic offset.

Figure C.4: The PSF' as a function of f_{hit} bins. For Mrk 421, only the first 6 energy bins (a-f) contained significant excess. Figure 5.11(c) shows the systematic offset between data and simulation. It is in rough agreement with the Crab simulation vs data comparison.

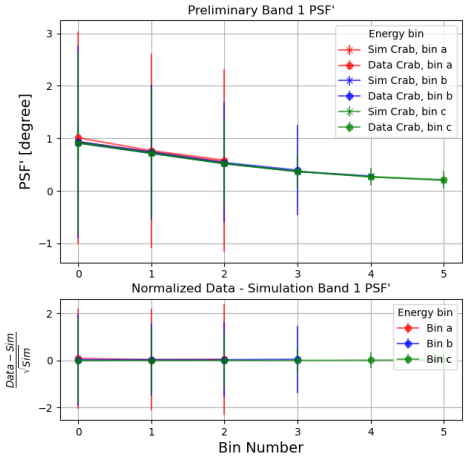

(a) First band.

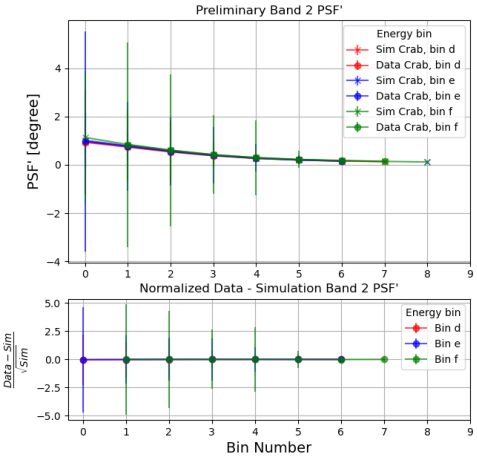

(b) Second band.

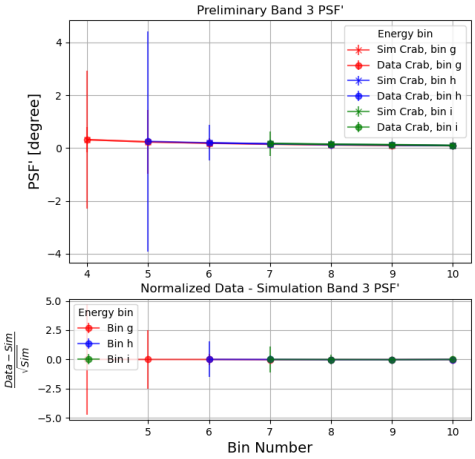

(c) Third band

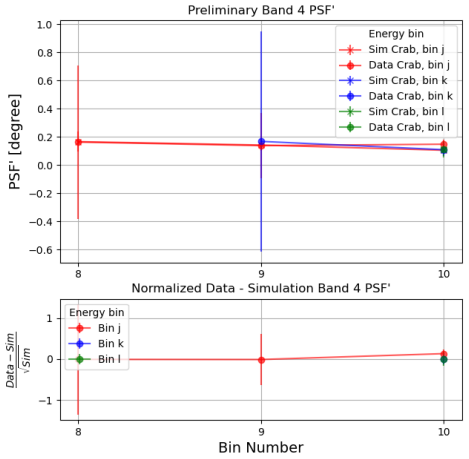

(d) Fourth band.

Figure C.5: The declination comparison of simulated PSF' between J2031+415 and Crab.

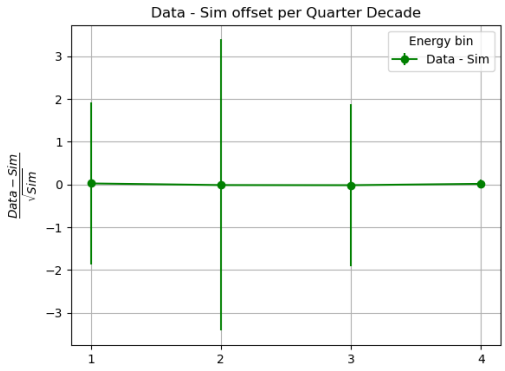

Figure C.6: Systematic normalized difference between simulated J2031+415 and Crab.

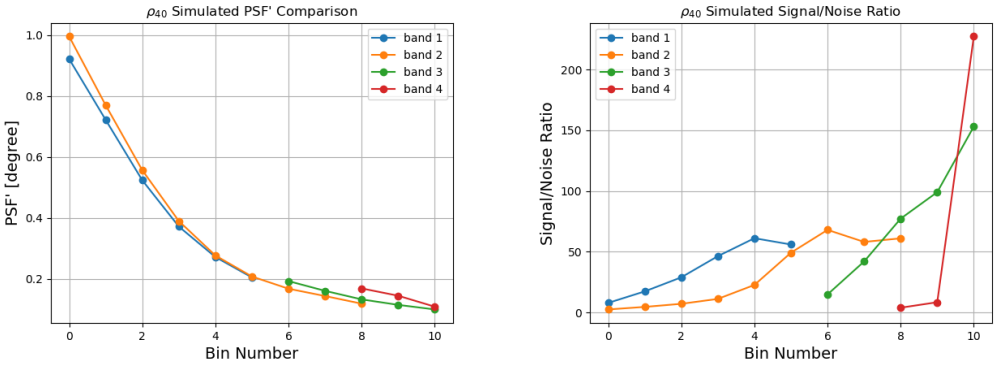

(a) Band PSF'.

(b) Band Signal/Noise Ratio.

Figure C.7: Simulated PSF' and signal/noise ratio for each energy band. This is done by combining each f_{hit} bin (an example would be bins B1C0Ea, B1C0Eb, and B1C0Ec in band 1) and performing a slice analysis on the new combined bin. This is to determine what bins contribute consistent statistics to the analysis.

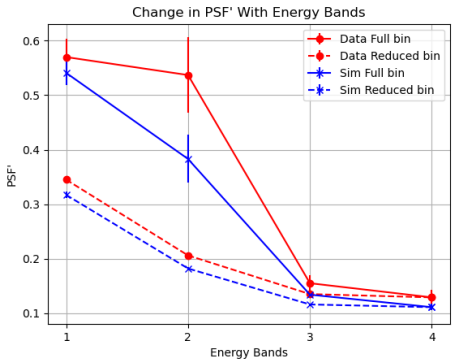

(a) Band PSF'.

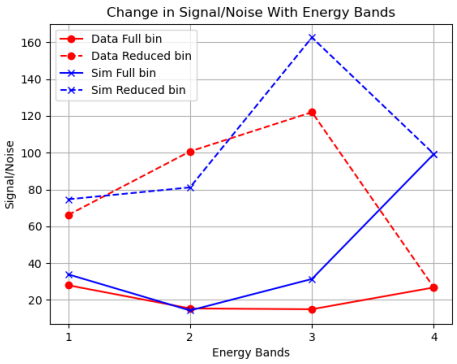

(b) Band Signal/Noise Ratio.

Figure C.8: Simulated PSF' and signal/noise ratio comparison for the full and reduced data along with simulated data. It can be seen that significant improvements are gained in both band PSF' and signal/noise, especially in the lower energy bands.

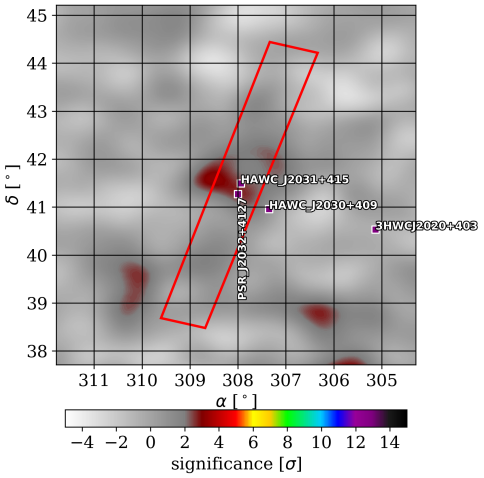

(a) First band significance map.

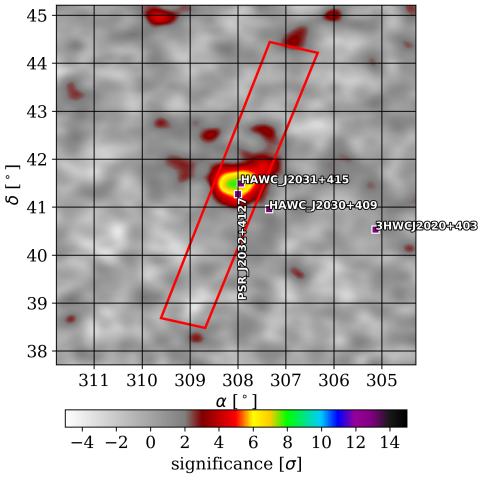

(b) Second band significance map.

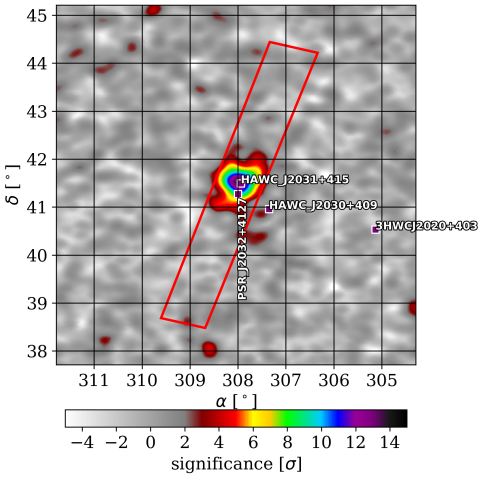

(c) Third band significance map.

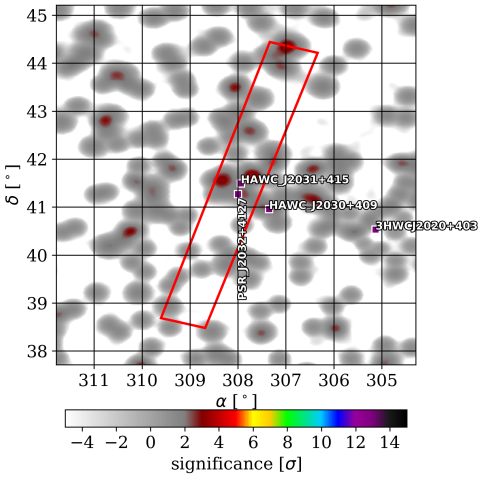

(d) Fourth band significance map.

Figure C.9: The significance maps for the ρ_{40} data set energy bands.

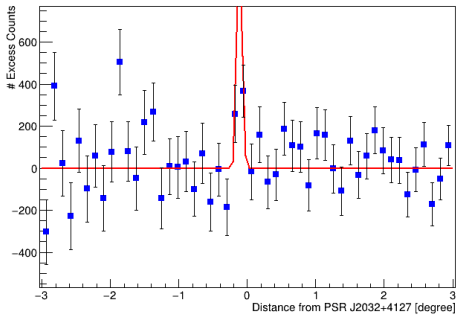

(a) First band excess count map.

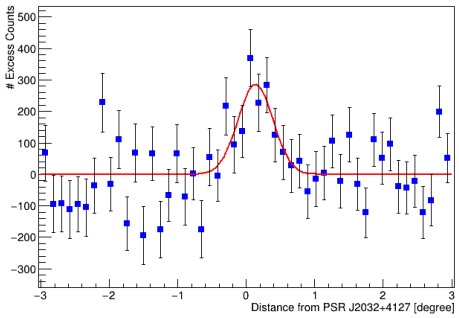

(b) Second band excess count map.

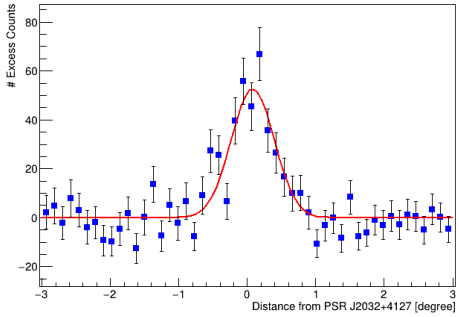

(c) Third band excess count map.

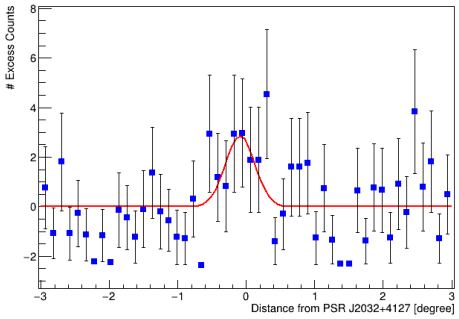

(d) Fourth band excess count map.

Figure C.10: Final excess count maps for the ρ_{40} isolated data set. Note the poor excess count profile for band 4. This is most probably due to the small overlap in the energy band definition and the energy range of J2031+415.